Generating a High-resolution Time-series Ocean Surface Net Radiation Product by Downscaling J-OFURO3

Jianglei Xu, Bo Jiang, Shunlin Liang, *Fellow, IEEE*, Xiuxia Li, Yezhe Wang, Jianghai Peng, Hongkai Chen, Hui Liang and Shaopeng Li

***Abstract*—The ocean surface net radiation (R_n) characterizing ocean surface radiation budget, is a key variable in ocean climate modeling and analysis. In this study, a downscaling scheme was developed to generate a high-resolution (0.05 °) time-series (2002 – 2013) daily ocean surface R_n from the third-generation Japanese Ocean Flux Data Sets with Use of Remote-Sensing Observations (J-OFURO3) at 0.25 ° based on the Advanced Very-High-Resolution Radiometer (AVHRR) top-of-atmosphere (TOA) observations (AVH021C) and other ancillary information (Clearness Index and cloud mask). This downscaling scheme includes the statistical downscaling models and the residual correction post-processing. A series of angle-dependent downscaling statistical models were established between the daily ocean surface R_n in J-OFURO3 and the AVHRR TOA data, and then, the residual correction was conducted to the model estimates R_n_AVHRR_est to obtain the final downscaled dataset R_n_AVHRR. Validation against the measurements from 57 moored buoy sites in six ocean observing networks shows the high accuracy of the downscaled estimates R_n_AVHRR_est with a R^2 of 0.88, RMSE of 23.44 $W \cdot m^{-2}$, and bias of -0.14 $W \cdot m^{-2}$ under all-sky condition. The results of the spatio-temporal analysis in R_n_AVHRR and inter-comparison with Cloud and the Earth's Radiant Energy System (CERES) and the Interim ECMWF Re-Analysis (ERA-Interim) products also indicated that the superior of the R_n_AVHRR with more detailed information especially in the hot spot regions, such as central tropical Pacific (warming pool), Atlantic and Equatorial Eastern Indian Ocean (EIO).**

***Index Terms*—AVHRR, downscaling, net radiation, ocean surface, remote sensing.**

This paragraph of the first footnote will contain the date on which you submitted your paper for review. This study was funded by the Chinese Grand Research Program on Climate Change and Response under the projects 2016YFA0600102, and National Natural Science Foundation of China (41971291). *(Corresponding author: Bo Jiang.)*

J. Xu. B. Jiang, X. Li, Y. Wang, J. Peng, H. Chen, H. Liang and S. Li are with the State Key Laboratory of Remote Sensing Science, Jointly Sponsored by Beijing Normal University and Institute of Remote Sensing and Digital Earth of Chinese Academy of Sciences, Beijing 100875, China, and also with the Beijing Engineering Research Center for Global Land Remote Sensing Products, Faculty of Geographical Science, Institute of Remote Sensing Science and Engineering, Beijing Normal University, Beijing 100875, China (e-mail: bojiang@bnu.edu.cn).

S. Liang is with the Department of Geographical Sciences, University of Maryland at College Park, College Park, MD 20742 USA, and also with the School of Remote Sensing and Information Engineering, Wuhan University, Wuhan 43079, China.

I. Introduction

THE ocean, as earth's primary heat reservoir, plays a crucial role in earth's energy budget and variations in ocean heat content, which makes a fundamental impact on regional and global climate system [1]. Through the transportation of general circulation in the ocean and atmosphere, heat, water, and momentum fluxes are frequently exchanged through the ocean surface to redress the heat imbalance. Generally, heat flux is transferred from atmosphere to the ocean by shortwave radiation, while it would be also lost by the longwave radiation emitting from the ocean to atmosphere. The ocean surface net radiation (R_n) characterizing ocean surface radiative energy budget balance is the difference between the downward and upward radiations from shortwave (0.3 μm ~3.0 μm) to longwave (3.0 μm ~100.0 μm) spectrum. During the day, a positive R_n value can be observed in most oceans [2], which means excessive energy is absorbed by the ocean surface and the sea surface temperature (SST) will increase subsequently. Part of this energy would be lost to the atmosphere through evapotranspiration (ET), while the remaining energy would be transferred to the full-deep ocean or cooler ocean regions through ocean currents to keep the ocean heat budget staying in a balance. The energy redistribution and interaction between ocean and atmosphere or in the ocean interior would ultimately influence the global and regional ocean climate systems [3]. For example, several studies have pointed out that some ocean climate events, such as typhoon, El Niño/Southern Oscillation phenomenon, etc., are closely related to ocean surface radiation anomaly [4, 5], especially the outgoing longwave radiation (OLR). Besides, the ocean surface radiation anomaly also leads to continental meteorological disasters, such as drought, rainstorm, etc. [6]. Therefore, ocean surface R_n information at various spatial scales is also necessary to help us to better understand the ocean climate system.

However, little attention has been paid to the R_n over ocean surface though it is vital for studies of surface energy exchange and ocean climate events. The voluntary observing ship (VOS) and moored buoy sites could provide the ocean surface radiation fluxes observations, but the available observations are few and sparsely distributed. The typical method to obtain the

ocean surface R_n was from the calculated radiative components (downward and upward shortwave and longwave radiation) which were computed by applying the bulk algorithms with a set of meteorological state variables (i.e., air temperature, sea surface temperature, sea surface humidity, sea surface wind, and so on) [7]. However, the accuracy and consistency of the calculated R_n from different bulk formulas vary a lot [8]. And this method is also limited to the spatial extent of application because it was developed based on the sparse meteorological measurements at point scale. Meanwhile, most inputted meteorological variables for the bulk algorithms are hardly obtained, which seriously hinders the development of the method [9, 10].

The alternative way to obtain the ocean surface R_n is from the existing datasets including the satellite-based product, the model reanalysis product, the reconstructed product, and the ship-based product. These products range from various spatial resolutions and temporal resolutions, as well as the long duration time periods, and are widely used [11-13]. Recently, Jiang *et al*. [14] validated and compared ten sets of ocean surface R_n products against the observations and pointed out their large discrepancies, which was consistent with the previous studies [12, 15, 16]. It was found [14] that the third generated Japanese Ocean Flux dataset with the Use of Remote Sensing Observations (J-OFURO3) performed best with the highest overall accuracy and the finest spatial resolution (0.25 °) than all other products. The J-OFURO3 project has offered daily ocean surface flux data sets that include heat, momentum, freshwater fluxes, and related parameters over the global oceans (except regions of sea ice) from 1988 to 2013. After a comprehensive analysis, the J-OFURO3 data was proved to be a good quality, which helps us to better understand ocean–atmosphere characteristics (such as ocean fronts, mesoscale eddies, and geographic features) and their effects on ocean climate change [17]. Even though, a dataset in ocean surface R_n with higher spatial resolution for analyzing the ocean climate events at local or regional scale is still required [18-20], and the frequent satellite observations at fine spatial resolution make it possible.

Downscaling methods are usually used to enhance the spatial resolution of a parameter without losing its original accuracy. The basic idea of these downscaling methods is to either establish a statistical correlation or develop a physically based model between aggregated high-resolution predictors and the targeted parameters at the coarse resolution scale, and then the developed downscaling model is applied in the high-resolution predictors to obtain targeted parameters at the fine scale. The type of input predictors (radar data, optical/thermal data, biophysical variables) and the characteristics of the scaling model (physical or statistical) are main differences of these downscaling methods [21]. Nowadays, the interest in statistical-based downscaling models development is growing because of its effectiveness and simplicity. Currently, different downscaling methods have been successfully applied in many fields, such as the soil moisture (SM) [22], the land surface temperature (LST) [23], the evapotranspiration [24], the precipitation [25] and so on. For example, Piles *et al*. [26] developed a downscaling statistical model to combine SM data from the Soil Moisture and Ocean Salinity (SMOS) and the fine-scale (1km) Moderate Resolution Imaging Spectroradiometer (MODIS) Normalized Difference Vegetation Index (NDVI) and the LST data, and then obtained the 1-km SM over Iberian Peninsula. The results showed that the spatial representation of SMOS coarse SM estimates was improved by the developed downscaling method while maintaining its temporal correlation. Hutengs *et al*. [27] proposed a downscaling method to the MODIS 1-km LST based on the random forest (RF) regression algorithm. In this study, the RF regression model was built between the MODIS LST and the topographical variables derived from the Shuttle Radar Topography Mission (SRTM), the MODIS land cover data, and the 250 m MODIS/Terra surface reflectance in the visible and near-infrared band, and then the 250 m LST estimates were calculated based on developed downscaling models. The result indicated that the method was promising for the downscaling of MODIS or VIIRS LST data. Mahour *et al*. [24] applied the downscaling cokriging method to retrieve the daily actual evapotranspiration (AET) with a medium spatial resolution (250m) from MODIS NDVI data, and the results showed AET had a higher spatial variability than original dataset. Therefore, the statistical based downscaling method was considered to be applied for downscaling the ocean surface R_n from J-OFURO3 into a finer spatial resolution using Advanced Very High Resolution Radiometer (AVHRR, 0.05 °) data in this study. The AVHRR sensor aboard National Oceanic and Atmosphere Administration (NOAA) polar-orbiting satellites was initially designed for meteorological applications and was proved to be a very powerful tool to monitor global surface. The earliest AVHRR sensor was aboard on TIROS-N in 1978, followed by NOAA-6/8/10 and the most recent satellites were NOAA-18/19 and Metop A/B, which constituted the longest global satellite observation record. Its characteristics include a high temporal frequency with a daily global coverage, a 4-km spatial resolution, and the presence of both visible and near-infrared (NIR) channels. These properties make it an attractive tool to study the evolution of atmospheric or surface variables at global scale [28, 29].

The main objective of this study is to develop a new statistical based downscaling scheme based on AVHRR data to retrieve a finer spatial resolution daily ocean surface R_n from J-OFURO3 dataset from 2002 to 2013. The organization of this paper was as follows. Section II gives a brief introduction of data and its pre-processing procedure. The details of the methods are provided in Section III, and the results are described in Section IV. Section V gives some uncertainties analysis. Conclusions are presented in Section VI.

II. Data and pre-processing

A. Moored Buoy Measurements

The ocean surface R_n measurements collected from 57 moored buoy sites in six ocean observing networks (details were shown in Table I) were used for accuracy validation in this study. These buoy sites are distributed over global oceans, and

TABLE I
INFORMATION OF THE SIX OBSERVING NETWORKS

Abbreviation	Site number	Observation frequency	Variables	Time span	URL
PIRATA	7	Daily	R_d^s, R_d^l, SST	2006166-2016350	http://www.pmel.noaa.gov/
RAMA	6	Daily	R_d^s, R_d^l, SST	2004297-2016350	http://www.pmel.noaa.gov/
TAO/TRITON	15	Daily	R_d^s, R_d^l, SST	2000113-2016350	http://www.pmel.noaa.gov/
OceanSITES	6	1h	R_d^s, R_d^l, SST	2000282-2018024	http://uop.whoi.edu/index.html
UOP	22	15min	R_d^s, R_d^l, SST	1991112-2016090	https://dods.ndbc.noaa.gov/oceansites/
CN-NADC	1	1h	R_d^s, R_d^l, R_u^s, R_u^l,	1999232-2014214	http://www.chinare.org.cn/

PIRATA: Pilot Research Moored Array in the Tropical Atlantic; RAMA: Research Moored Array for Afrcian-Asian-Austrian Monsoon; TAO: Tropical Atmosphere Ocean/Triangle Trans-Ocean Buoy Network; OceanSITES: Ocean Sustained Inter-disciplinary Timeseries Environment; UOP: Upper Ocean Process Group; CN-NADC: Chines National Arctic and Antarctic Center.

mostly over the low- to mid- latitude oceans, as shown in Fig. 1. The Global Ocean Observing System (GOOS), Global Climate Observing System (GCOS), and the Global Earth Observing System of Systems (GEOSS) together form the Global Tropical Moored Array Program. Major components of the program include Tropical Atmosphere Ocean/Triangle Trans-Ocean Buoy Network (TAO/TRITON) array in the Pacific [30], Pilot Research Moored Array in the Tropical Atlantic (PIRATA) in the Atlantic [31], and Research Moored Array for Afrcian-Asian-Austrian Monsoon (RAMA) in the Indian Ocean [31, 32]. OceanSITES is an integral part of the GOOS. Its observations cover meteorology, oceanography, water, biogeochemical, and cycle parameters associated with carbon, ocean acidification ecosystem and geophysics. The primary focus of Upper Ocean Process Group (UOP) is the study of physical processes in the upper ocean and at the air-sea interface using moored surface buoys equipped with meteorological and oceanographic sensors [33]. The Chinese National Arctic and Antarctic Center (CN-NADC) is a national facility within the Polar research institute of China (PRIC). It serves as the only authorized institution in China to capture, regulate the management and long-term preservation of data and sample information, and provide sustainable polar data service. The available data generally covers physical oceanography, marine meteorology, polar marine chemistry and so on [34].

However, ocean surface R_n was not the routine measurements at most moored buoy sites, instead of the downward shortwave radiation, downward longwave radiation, and sea-surface temperature (except the site in CN-NADC) being available. Therefore, ocean surface R_n was calculated firstly at each buoy site according to the following:

$$R_n = R_n^s + R_n^l \quad (1)$$

$$R_n^s = (1 - \alpha_{sw})R_d^s \quad (2)$$

$$R_n^l = R_d^l - R_u^l = R_d^l - \left[\varepsilon_{ocean}\sigma SST^4 + (1 - \varepsilon_{ocean})R_d^l\right] \quad (3)$$

where R_n^s is the net shortwave radiation (W ㎡$^{-2}$), R_n^l is the net longwave radiation (W ㎡$^{-2}$), α_{sw} is the daily ocean surface shortwave broadband albedo provided by Global LAnd Surface Satellite (GLASS) team [35], R_d^s is the shortwave downward radiation on the ocean surface (W ㎡$^{-2}$), R_d^l and R_u^l are the downward and upwelling longwave radiation at the ocean surface (W ㎡$^{-2}$), ε_{ocean} is the daily ocean surface broadband emissivity, provided by the GLASS team [36], *SST* is the sea surface temperature (unit: K), and σ is Stefan-Boltzmann's constant ($5.67 \times 10^{-8} W \cdot (m^{-2} \cdot K^{-4})$).

Table I provides the detailed information of each network. It was seen that these moored buoy measurements from various networks have different temporal resolutions, units and data formats, hence, a strict pre-processing procedure was conducted in order to keep the consistency of these measurements. First of all, all measurements were used only when their quality code labeled as 1 (high quality) [37], and then, the daily R_n was directly calculated according to Eqs.(1)-(3) at the sites from PIRATA, RAMA, and TAO/TRITON. For those sites that sampling resolution was less than daily, their measurements were firstly processed into hourly scale, and the daily R_n was calculated by averaging the hourly records only if at least one observation was available in each single hour for one day. Unit of measurement was unified to W·m^{-2}. Afterwards, time-series data for each buoy sites was quality controlled by visual inspection and three-sigma rule [38] so as to exclude the abnormal records. Finally, all these daily R_n measurements (14,688 samples for clear-sky and 30,695 for cloudy-sky) from buoy sites were used for validation in this study.

B. Remotely Sensed Data

1) AVH02C1: The Land Long-Term Data Record Project (LTDR: http://ltdr.nascom.nasa.gov/) provides the Version5 of the AVHRR Top-of-Atmosphere (TOA) reflectance/brightness temperature data (AVH02C1) (bands 1-5) used in this study. The consistent AVHRR dataset generated from global area coverage (GAC) data has a spatial resolution of 0.05 ° at daily scale (one instantaneous observation per day) from 1981 to present based on AVHRR sensor [39]. These AVHRR TOA Observations provide five spectral bands at visible channel (0.580-0.680 μm), near-infrared channel (0.725-1.100 μm), mid-infrared channel (3.55-3.93 μm) and thermal channels (10.5-11.3 um, 11.5-12.5 μm). However, the AVHRR instrument suffered from the lack of onboard calibration for its visible to shortwave infrared channels, therefore, the LTDR project adopted the approach developed by Vermote [40] which relies on the clear ocean and accurate Rayleigh scattering computations to derive the sensor degradation in the red bands consistently across the AVHRR instruments onboard various NOAA satellites. In particular, the calibrated method consists

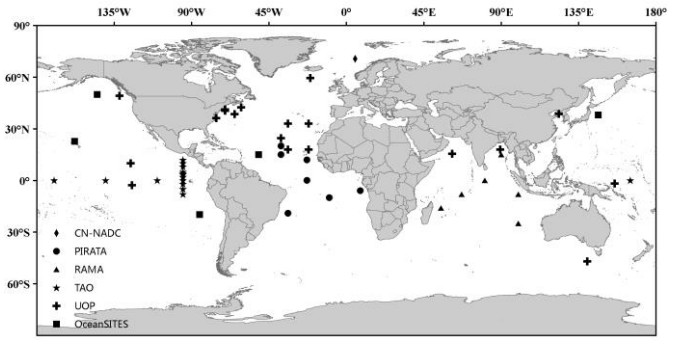

Fig. 1. Global ocean distribution of six observing networks.

of two steps. The first step is to use bright clouds at high latitudes (12 kilometers and above) as "white" targets to perform inter-calibration between channels 1 and 2, which has a comparable function with that using ocean glint. The second step is to perform an absolute calibration of channel 1, using an offshore nadir view (40-70 °) at channels 1 and 2, and to correct the aerosol effect. In this process, the satellite measurements in channel 2 are used to depress the aerosol effect in the channel 1 after the water vapor absorption correction. In turn, the net signal in channel 1, consisting of the predictable Rayleigh scattering component, is used to calibrate this channel itself. Meanwhile, a clock correction approach [41] was also applied for a better geolocation correction to AVH02C1 dataset. The corresponding geometric information (i.e., solar zenith angle (SZA), viewing zenith angle (VZA), and relative azimuth angle (RAA)) for each pixel were extracted. Besides, the corresponding AVHRR cloud mask data which matches well with MODIS cloud mask at a consistency greater than 90% [42], was used to identify the different sky conditions. It is noting that the missing data in AVH02C1 is most in mid- and low-latitude areas. The pre-processing procedure is below.

At first, the TOA observations (0.05 °) from AVH02C1 were aggregated into 0.25 ° scale to match ocean surface R_n from J-OFURO3. Instead of directly averaging within each window (5×5 pixel) in the visible/near-infrared bands (bands 1-2), the SZA for every pixel in this window was also incorporated according to Pinker [43] as Eq. (4) shows, while the brightness temperature data (bands 3-5) was directly averaging. Afterwards, the averaged TOA observations in *i*th channel $\bar{r}_{toa_i}$ were used to develop the downscaling model.

$$\bar{r}_{toa_i} = \sum_{j=1}^{25} \left(\frac{(r_{toa_{i,j}})^2}{cos(\theta_{s_j})} \right) \Big/ 25 \quad (4)$$

where $r_{toa_{i,j}}$, θ_{s_j} are *j*th TOA visible/near-infrared observation and its SZA (unit: °) extracted from AVH02C1 within each window in *i*th channel (*i*=1, 2), respectively. Moreover, only the pure clear- or cloud-sky samples from J-OFURO3 were considered in this study, which was determined only when 25 AVH02C1 pixels within one window were all labeled as clear (cloud mask = 0) or cloud (cloud mask = 1).

2) J-OFURO3: J-OFURO3, a third-generation data set developed by the Japanese Ocean Flux Data Sets with Use of Remote-Sensing Observations (https://j-ofuro.scc.u-tokai.ac.jp/en/) research project. The initial data set, J-OFURO1 was released to the public around 2000; the second-generation data set, J-OFURO2, followed closely behind in 2008, and its main featured improvements primarily steamed from using multi-satellite data. In order to further improve the quality of dataset, a variety of follow-up research and development were conducted to construct the third-generation, J-OFURO3, which offers datasets for surface heat, momentum, freshwater fluxes, and related parameters over the global oceans (except sea ice covered regions) from 1988 to 2013, based on a 0.25 grid system at daily scale [44]. J-OFURO3 provides daily ocean surface R_n^s and R_n^l [17]. Specifically, the R_n^s was calculated by Eq. (2), in which the R_d^s was interpolated from the International Satellite Cloud Climatology Project (ISCCP) (before 2000) and the version 3A of CERES Synoptic data (CERES-SYN1deg_Ed3A) (after 2000) and the α_{sw} was set as 0.03. While the R_n^l was calculated by Eq. (3), in which the R_d^l was also interpolated from ISCCP [45] (before 2000) and CERES-SYN1deg_Ed3A (after 2000) and the R_u^l was calculated with the emissivity (set as 0.975) and *SST* from J-OFURO3. Then, the ocean surface R_n was obtained by combing daily ocean surface R_n^s and R_n^l. R_n_JOFURO3 from 2002 to 2013 was used for downscaling modelling.

3) CERES-SYN1deg: Cloud and the Earth's radiant Energy System (CERES: https://ceres.larc.nasa.gov/index.php) is a broadband instrument measuring both solar-reflected shortwave and earth-emitted longwave radiation from TOA to the earth surface, onboard on Terra, Aqua and the Suomi National Polar-orbiting Partnership (S-NPP) satellites, with 20-km spatial resolution at nadir [46]. CERES flux product was regarded as one of the most advanced flux product [47]. So the CERES surface radiation flux data was taken as the reference in this study. The version 4A of CERES Synoptic products (CERES-SYN1deg_Ed4A) data was used. CERES-SYN1deg_Ed4A was calculated using the Langley Fu-Liou radiative transfer model from the input geostationary (GEO) radiance, Moderate Resolution Imaging Spectroradiometer (MODIS) and GEO cloud properties, Goddard Modeling and Assimilation Office (GMAO) atmospheric profiles, and MODIS aerosols [48]. Compared to SYN1deg_Ed3A, SYN1deg_Ed4A has many algorithm and input improvements. In Ed3A, MODIS Collection 4 was switched to Collection 5 at the end of March 2006, and the switch caused a shift in the retrieved aerosol optical thickness over land. While, in Ed4A, MODIS Collection 5 was used from March 2000 through February 2017, and Collection 6 was used for March 2017, so the shift was eliminated. Both the MODIS and GEO cloud retrieval algorithms were significantly improved in Edition 4A, and cloud properties from geostationary satellites were derived hourly, which further improved the temporal resolution from the 3-hourly in SYN1deg_Ed3A to hourly in SYN1deg_Ed4A. Besides, there are also many other improvements which can be found in CERES SYN1deg_Ed4A Data Quality Summary. Therefore, the ocean surface R_n data from CERES-SYN1deg_Ed4A (R_n_CERES, hereinafter) was obtained by combining the four radiative components (downward and

upward shortwave and longwave radiation) with 1 ° spatial resolution at daily scale.

C. Reanalysis Data

The European Center for Medium range Weather Forecasting (ECMWF: https://apps.ecmwf.int/) has released a reanalysis data ERA-Interim aiming at replacing ERA-40. ERA-Interim uses 4D-variational analysis (4D-var) that is a temporal extension of 3D-var on a spectral grid with triangular truncation of 255 waves (corresponds to approximately 80 km spatial resolution) and a hybrid vertical coordinate system with 60 levels [49]. Its radiation is calculated based on the Rapid Radiation Transfer Model (RRTM). ERA-Interim data covers period from 1989 to present at a horizontal spatial resolution of 0.75 °over globe at 6-hourly interval. ERA-Interim is usually as a reference data in many radiation studies [50-52], and it was thought to be better than other reanalysis product in ocean surface radiation [14], therefore, ocean surface R_n data from ERA-Interim was also used as a reference in this study.

D. Other Parameters

The AVHRR TOA data was used to downscale the daily R_n_JOFURO3, however, it is far from enough to describe the daily average atmospheric condition only depending on one instantaneous TOA observation per day. Several studies have applied the instantaneous TOA satellite observations to estimate daily surface radiation by assuming the atmospheric conditions were invariant during a day [53-55]. However, this assumption was found to be unreasonable in our previous research, and the clearness index (CI) was suggested to present the daily atmospheric transmittance [56]. CI has been successfully applied to several related studies [57, 58] and it can be calculated as following:

$$\mathrm{CI} = {R_d^s}\Big/{DSR_{toa}} \tag{5}$$

where R_d^s is extracted from CERES SYN1deg_Ed4A data, DSR_{toa} is the TOA shortwave downward radiation calculated through Eqs. (6)-(9) [59].

$$DSR_{toa} = \frac{1440 G_{sc} d_r}{\pi}(\omega_s \sin\varphi \sin\delta + \cos\delta \sin\omega_s) \tag{6}$$

$$d_r = 1 + 0.033 \cos\left(\frac{2\pi DOY}{365}\right) \tag{7}$$

$$\omega_s = \cos^{-1}(-\tan\varphi \tan\delta) \tag{8}$$

$$\delta = 0.409 \sin\left(\frac{2\pi DOY}{365} - 1.39\right) \tag{9}$$

where G_{sc} is the solar constant (0.0820 MJm^{-2} min^{-1}); d_r is the distance between earth and sun; ω_s, φ and δ are hour angle, latitude and sun declination, respectively. The calculated CI was sampled into 0.25 ° using the nearest neighboring interpolation to match the spatial resolution of R_n_JOFURO3.

III. METHODOLOGY

Figure 2 gives the overall flowchart of this study. It contains four steps. The first step, the qualified comprehensive R_n_JOFURO3 samples were selected based on the filter results between J-OFURO3 and CERES-SYN1deg_Ed4A data. The second, all inputs were extracted according to the selected samples and pre-processed subsequently. Thirdly, the downscaling models were developed based on the AVHRR TOA data under various conditions (i.e., geometric combination, sky conditions) and validated against the measurements collected from the moored buoy sites. And the residual correction method was applied at the last step to the estimates derived from step 3 to generate a more accurate and reliable estimates. Three measures were used to characterize the validation accuracy: R^2, root-mean-square-error (RMSE), and bias. In general, all three measures were examined to evaluate the performance of various models, but RMSE values were given larger weights. More details about these major steps were given below.

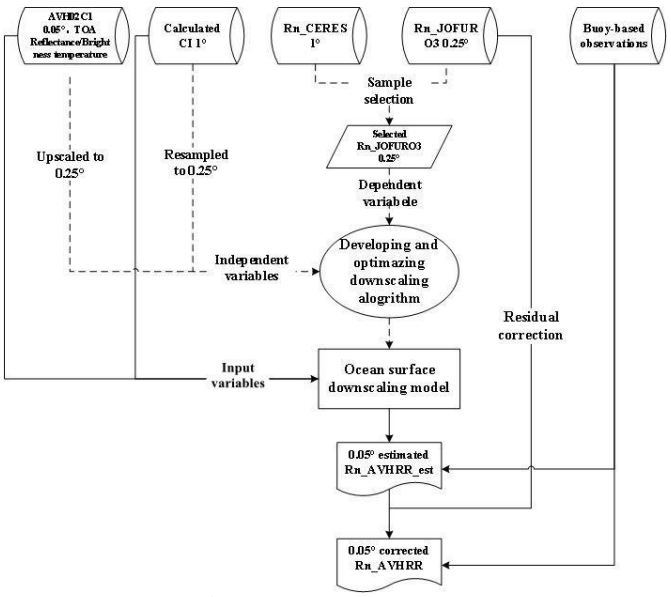

Fig. 2. Flowchart of downscaling R_n_JOFURO3 using AVHRR data.

A. Samples Selection

To obtain the most representative R_n_JOFURO3 data with a good quality, a test about data consistency was conducted taking the corresponding R_n_CERES as the reference because of the satisfactory performance of CERES radiation over land and ocean surface [14, 60]. First of all, R_n_JOFURO3 data was aggregated into 1 ° (4 × 4 pixels in one window) to match the R_n_CERES. And then, a multi-year absolute difference between R_n_CERES and the aggregated R_n_JOFURO3 was calculated for each sample. Based on the statistical results, it showed that more than 60% of the difference values were within 1 $W{\cdot}m^{-2}$, which agreed well with the validation accuracy in Jiang's study [14] (bias = 0.742 $W.m^{-2}$). Hence, 1 $W{\cdot}m^{-2}$ was taken as the spatial threshold to select the aggregated R_n_JOFURO3 samples by Eq. (10):

$$\left|Rn_f^a - Rn_C\right| < 1 \tag{10}$$

where Rn_f^a is the aggregated R_n_JOFURO3 (1 °), Rn_C is the corresponding R_n_CERES.

Each selected Rn_f^a contains 16 original R_n_JOFURO3 pixels, which were examined by the Tuckey's Test [61] to ensure their consistency. In Tuckey's test, the minimum and maximum

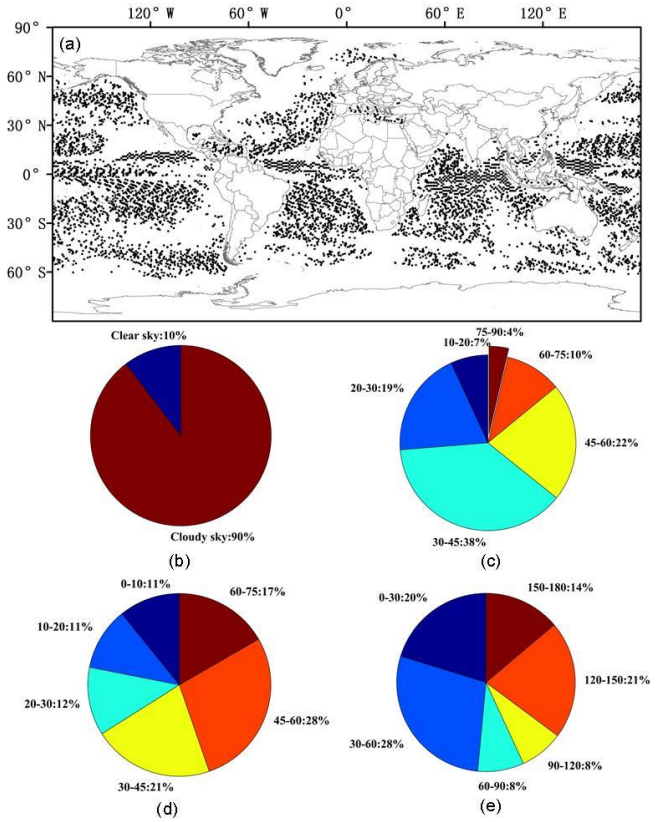

Fig. 3. Distribution of the selected samples from R_n_JOFURO3 over global oceans (a), and under different sky (b), SZA (c), VZA (d) and RAA (e) conditions, respectively.

TABLE II
SUMMARY OF THE INDEPENDENT AND RESPONSE VARIABLES IN THE DOWNSCALING MODELS

	Abbr	Full Name	Unit	Data source	Processing
Response variable	Rn_J	Ocean surface R_n	W·m^2	J-OFURO3	\
Independent variable	r_{toa}	TOA reflectance	\	AVH02C1 (bands 1-2)	Eq.4
	t_{toa}	TOA brightness temperature	K	AVH02C1 (bands 3-5)	Averaging
	CI	Clearness Index	\	Calculated	Nearest neighboring interpolation
	lat	Latitude	Degree	J-OFURO3	\
	doy	Julian day	\	J-OFURO3	\

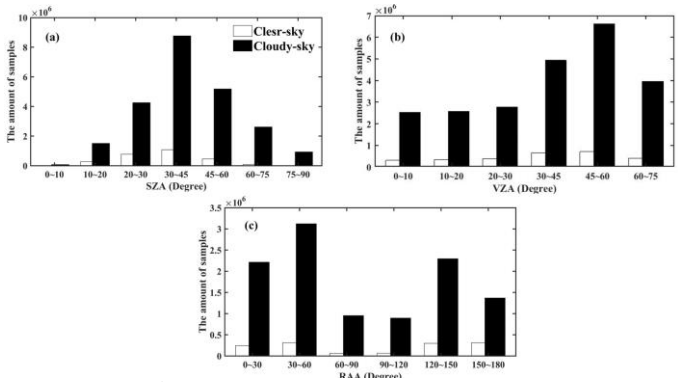

Fig. 4. Number of samples in each bin composed by (a) SZA, (b) VZA, and (c) RAA under clear- and cloudy-sky, respectively. The X-axis in each plot gives the corresponding range of each bin.

values ($R_{n_{min}}$, $R_{n_{max}}$) for each window in Rn_J^a sample were first calculated by Eqs. (11) and (12), and then the pixels in this window were excluded as long as their values exceed the range between $R_{n_{min}}$ and $R_{n_{max}}$. Moreover, the information about location and time of each pixel was also examined to make the samples more representative and comprehensive.

$$R_{n_{min}} = q1 - k \times (q3 - q1) \quad (11)$$
$$R_{n_{max}} = q3 + k \times (q3 - q1) \quad (12)$$

where $q1$ is the lower quartile; $q3$ is the upper quartile; k is a coefficient defined as 1.5 in our study [62].

Finally, 6,101 points from 2002 to 2013 (26,051,451 samples in total) in R_n_JOFURO3 over global ocean were selected for modelling (Fig. 3a) in this study period.

B. Downscaling Models Development

A series of the statistical downscaling models were developed to downscale the R_n_JOFURO3 with the AVH02C1 data and other ancillary information under various conditions. Table II gives the response and independent variables used for modeling. According to previous studies [55], the different conditions were defined by the angle bin groups composed with SZA, VZA and RAA as well as the atmospheric conditions (clear- / cloudy-sky) determined based on the AVH02C1 cloud mask in this study and the number of samples in each bin was shown in Fig. 4. For clarify, Fig. 3b-e gives the proportion distribution of the selected samples under different conditions. It was shown that the SZA range of these samples is mainly from 20 ° to 75 ° both in clear- and cloudy-sky, while the distributions of the VZA and RAA were relatively uniform. Besides, the samples were mainly in cloudy-sky (Fig. 3b), which means the cloudy day was very often over oceans. Noting that these models were built only when the number of samples was larger than 100. Therefore, 504 (7 SZA bins * 6 VZA bins * 6 RAA bins * 2 sky conditions) downscaling conditional models should be built theoretically, however, only 297 models were developed because of the limitation of sample size (> 100), in which 127 models were under clear-sky condition and 170 models were under cloudy-sky condition, respectively. In the development of downscaling regression models, the training dataset of each bin was randomly divided into two subsets that 80% was used for model training and the remaining 20% was used for model validation.

The mathematic format of the downscaling regression models was shown in Eq. (13):

$$Rn_J = f_{\theta_s,\theta_v,\varphi}(r_{toa}, t_{toa}, CI, lat, doy) \quad (13)$$

The explanations of each variable and corresponding processing were given in Table II. Under the assumption that the TOA observations of each AVH021C pixel in the 5*5 window corresponding to one R_n_JOFURO3 sample have the same relationship with its ocean surface R_n, hence, the downscaling models were developed at each samples directly,

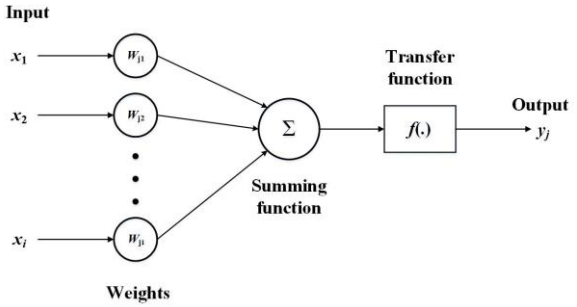

Fig. 5. Schematic diagram of a neuron.

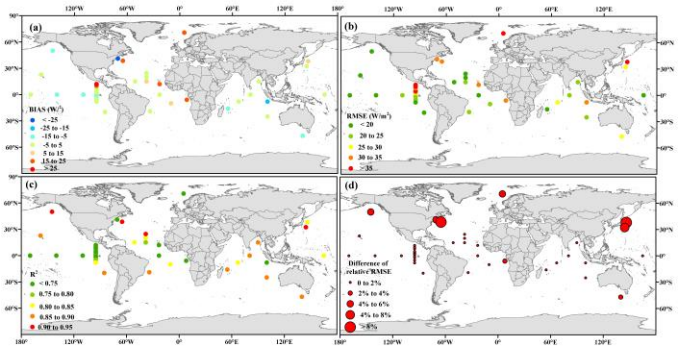

Fig. 7. Spatial distribution of the R_n_AVHRR_est validation results at each buoy site: (a) BIAS (Wm^{-2}), (b) RMSE (Wm^{-2}), (c) R^2 and (d) the difference of relative RMSE values between R_n_AVHRR_est and R_n_JOFURO3 against buoy observations.

and all independent variables (except latitude and Julian day) were pre-processed into 0.25° (see Section II).

Artificial neural network (ANN) is a powerful regression modelling tool that is used widely [63]. It can learn the relationship between inputs and outputs by studying previously recorded data [64]. Generally, a typical neural network consists of an input layer, a hidden layer, an output layer, and other associated components include neurons, weights and transfer functions, etc. Fig. 5 shows a typical neuron in a neural network. Back-propagation (BP) [65] is one of the available forms of neural networks. Besides, there are different training algorithms associated with it, such as Gradient descent and Levenberg-Marquardt [63]. In general, BP algorithm is ideal for multi-layer feedforward neural networks.

A key step to build an efficient ANN model is to find the optimal architecture including the number of layers, the number of neurons in each layer, and the transition functions associated with each neuron [66]. It was concluded that a three-layer network with tan-sigmoid transfer functions in the hidden layer and linear function in other two layers was enough for most modelling applications [63], hence, it was also applied in this study. However, the most important thing was to determine the optimal number of neurons in the hidden layer for each downscaling model in this study. The optimal state was determined when the absolute deviation of the RMSE values between connected neurons was all less than 0.01 with 5 consecutive neurons. The number of neurons corresponding to the minimum RMSE value was the optimal number of neurons in the hidden layer of the model. The optimal structure of each model was determined one by one, and it was found that 20 to 25 was the general number of optimal neurons for most cases.

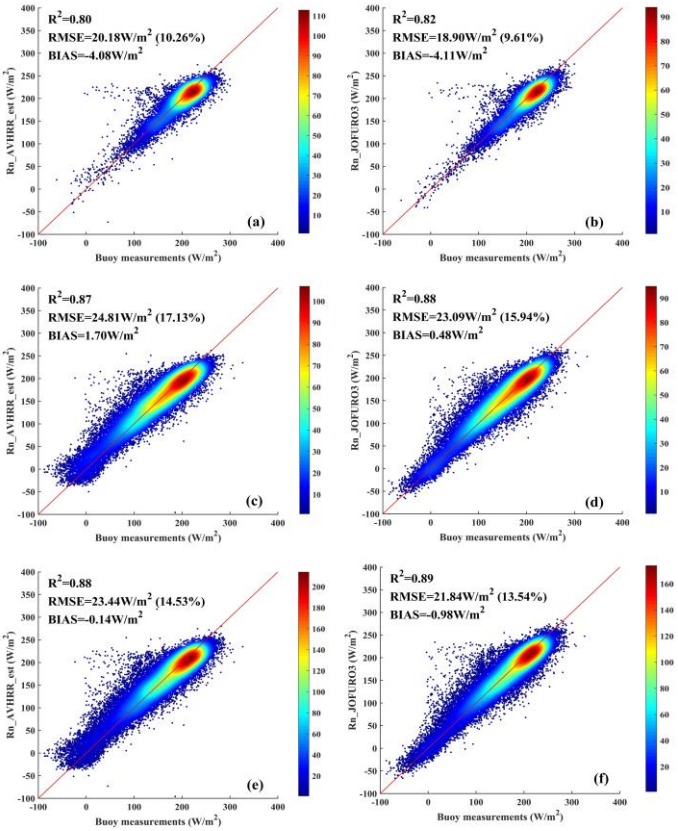

Fig. 6. The validation results of R_n_AVHRR_est and R_n_JOFURO3 against buoy measurements from 2002 to 2013 under clear sky (a-b), cloudy sky (c-d), all-sky (e-f) conditions, respectively.

Afterwards, these downscaling models were used to calculate the ocean surface R_n estimates at high spatial resolution of 0.05 ° (R_n_AVHRR_est, hereinafter) with the original AVHRR TOA observations as input. And then, the R_n_AVHRR_est at 0.05° was validated against all moored buoy measurements.

C. *Residual Correction*

A residual correction was applied to the estimates from the downscaling models because the developed ANN regression models cannot account for the total variation in the original data with a coarse resolution [27]. The residual correction proposed by Kustas [67] has been applied frequently in previous downscaling works [68, 69]. It is to use the information of original coarse resolution data to scale the range of the downscaled data to a normal one matching the coarse resolution data. In this study, the residual correction consists of three steps: First, the estimated R_n_AVHRR_est (0.05 °) values from the downscaling models were aggregated into 0.25 ° (5×5 pixel in one window) to match the original R_n_JOFURO3. Secondly, the residuals between the aggregated R_n_AVHRR_est and the corresponding R_n_JOFURO3 were calculated. Thirdly, the residuals were resampled into 0.05 ° and then added to each R_n_AVHRR_est in the aggregated window to yield the final corrected result (R_n_AVHRR, hereinafter). The procedure is indicated as below:

$$\Delta R_{n0.25} = Rn_J - \hat{R}_{n0.25} \quad (14)$$

$$\Delta R_{n0.05} = f(\Delta R_{n0.25}) \quad (15)$$

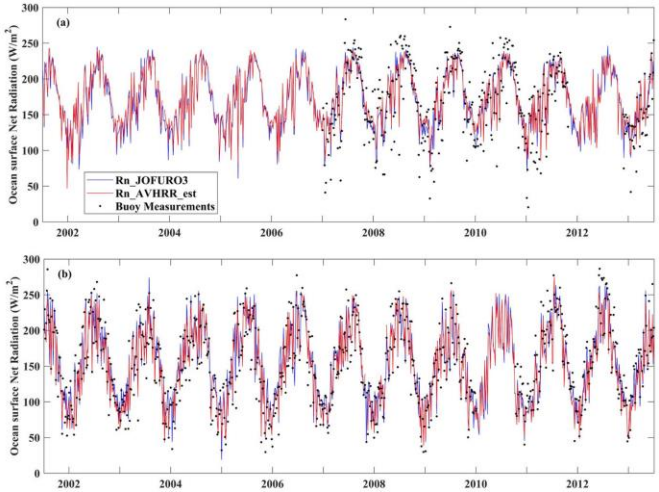

Fig. 8. Temporal variations in R_n_AVHRR_est , R_n_JOFURO3, and buoy measurements at sites (a) PIRATA_03 (10 ℃S, 10 ℃W) and (b) OceanSITE_STRATUE (19.75 ℃S, 85.33 ℃W).

$$\hat{R}_{n0.05} = R_{n0.05} + \Delta R_{n0.05} \quad (16)$$

where Rn_J is the R_n_JOFURO3, $\hat{R}_{n0.25}$ is the aggregated R_n_AVHRR_est, $R_{n0.05}$ is the R_n_AVHRR_est, $\Delta R_{n0.25}$ and $\Delta R_{n0.05}$ is the residual and resampled residual, respectively, $\hat{R}_{n0.05}$ is the R_n_AVHRR.

The residual correction can ensure that the re-aggregated downscaled R_n matches the original coarse resolution data and remove some prediction bias. However, if the downscaling model's predictive strength is low, notable boxshaped artifacts may, on the other hand, be introduced into the downscaled R_n map [70].

IV. RESULTS

Downscaling Results Validation

The R_n_AVHRR_est estimates from downscaling models under clear- and cloudy-sky conditions were directly validated (14,688 validated samples for clear-sky and 30,695 for cloudy-sky) using the measurements from 57 moored buoy sites separately, and the corresponding validation results of R_n_JOFURO3 were also calculated for comparison, and all results were displayed in Fig. 6. R_n_AVHRR_est estimates showed a good agreement with buoy observations with RMSEs of 20.18 W·m^{-2}, 24.81 W·m^{-2} and 23.44 W·m^{-2}, biases of -4.08 W·m^{-2}, 1.70 W·m^{-2} and -0.14 W·m^{-2}, R^2 of 0.80, 0.87 and 0.88 under clear-sky, cloudy-sky and all-sky, respectively. Generally, the downscaled results have the tendency to be underestimated under clear-sky, while overestimated under cloudy-sky, respectively. It was also observed that the underestimation at high values (>250 W·m^{-2}) and overestimation at low values (<0 W·m^{-2}) in R_n_AVHRR_est occurred under both clear-sky and cloudy-sky conditions. Comparatively, the overall accuracy of R_n_JOFURO3 was close to R_n_AVHRR_est with RMSEs of 21.84 W·m^{-2}, 18.90 W·m^{-2} and 23.09 W·m^{-2}, biases of -0.98 W·m^{-2}, -4.11 W·m^{-2} and 0.48 W·m^{-2}, and R^2 of 0.89, 0.82 and 0.88 under all-, clear- and cloudy-sky, respectively. The relative RMSE values of R_n_AVHRR_est comparing to R_n_JOFURO3 increased by 0.65% (from 9.61% to 10.26%), and 1.19% (from 15.94% to 17.13%) under clear- and cloudy-sky, separately,

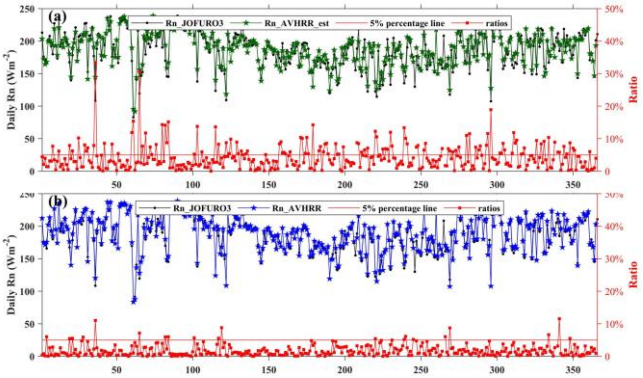

Fig. 9. Times series plots of downscaled ocean surface R_n and J-OFURO3 for (a) uncorrected case and (b) corrected case at site TAO_01 (0 °, 95 ℃W). Ratio (%) is the relative difference between R_n_AVHRR_est or R_n_AVHRR and J-OFURO3.

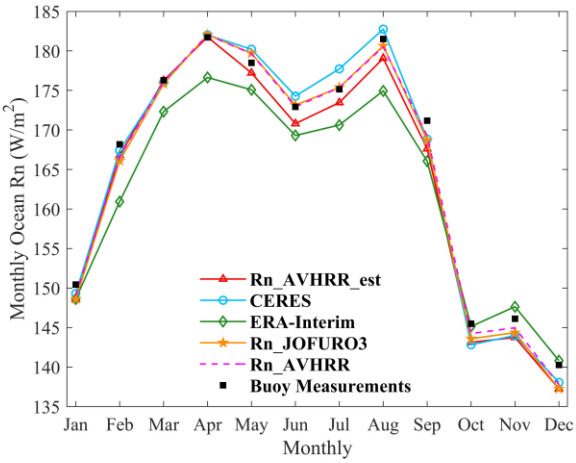

Fig. 11. Monthly variations in R_n_AVHRR_est, R_n_AVHRR, R_n_CERES, R_n_J-OFURO3, R_n_ERA-Interim and buoy observations from 2002 to 2013.

which means that the downscaling models performed better under clear-sky than that under cloudy-sky resulted from the overestimation at low values. It was possibly due to the uncertainty of the AVHRR cloud mask resulting in poorer performance under cloudy-sky. Overall, the validation results indicated that the performances of the new developed downscaling models for daily ocean surface R_n are satisfactory.

According to statistics, the mean RMSE values of OceanSITE, PIRATA, RAMA, TAO and UOP networks were 23.38 W·m^{-2}, 24.07 W·m^{-2}, 24.62 W·m^{-2}, 27.86 W·m^{-2} and 28.32 W·m^{-2}, respectively. In general, the accuracy of R_n_AVHRR_est was satisfactory and comparable with R_n_JOFURO3 at low latitude open sea buoy sites, such as PIRATA, RAMA and TAO in the tropical oceans. Figure 7 represents the spatial distribution of the validation results of the R_n_AVHRR_est at each moored buoy site. Fig. 7a and b also show that the accurate R_n_AVHRR_est estimates were mostly at the buoy sites in open the seas, while the poor R_n_AVHRR_est estimates were usually at the buoy sites in the coastal or high latitude oceans with a larger RMSE or bias magnitude. For comparison, the difference of the relative RMSE values between the R_n_AVHRR_est and the R_n_JOFURO3 of each buoy site were calculated and shown in Fig. 7d, and the larger values mean the difference between the

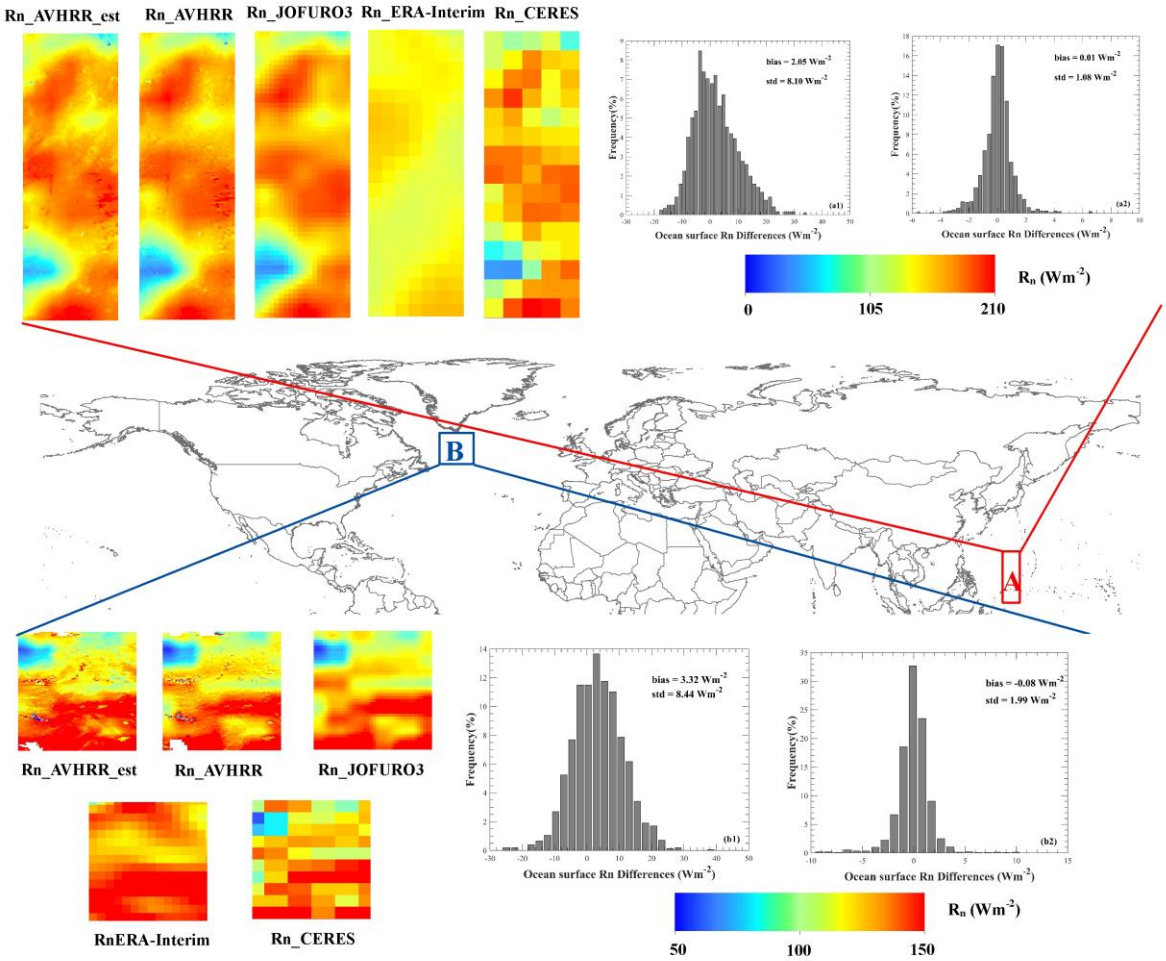

Fig. 10. Comparison of R_n_AVHRR_est (0.05 °), R_n_AVHRR (0.05 °), R_n_JOFURO3 (0.25 °), R_n_ERA-Interim (0.7 °) and R_n_CERES (1 °) at 225 day of 2008 in study area A (Lat: 5 ° N ~ 20 °N, Lon: 135 °E ~ 140 °E) and study area B (Lat: 50 ° N ~ 60 °N, Lon: 35 °W ~ 45 °W). (a1) and (b1) are the differences between R_n_AVHRR_est and R_n_JOFURO3 over A and B study areas. (a2) and (b2) are the differences between R_n_AVHRR and R_n_JOFURO3 over A and B study areas. White color represents the missing data.

R_n_AVHRR_est and the R_n_JOFURO3 was large. It was observed that the differences were remarkable at some buoy sites in the coastal and high latitude oceans, such as the buoy sites in UOP network closer to the coastal area and the site CNNADC_NWsea (70.66 °N, 5.1 °E) with the largest RMSE value (60.25 $W \cdot m^{-2}$) located in the Arctic seas. It was noting that the R_n_JOFURO3 pixels in the coastal areas were extrapolated from nearby pixels without sufficient quality checks [71], even though no satellite observations were available [72], thus, the R_n_JOFURO3 performed worse in the coastal areas. Besides, the increased surface heterogeneity in the process of aggregation and downscaling near the coast, and the complex air-sea interactions influenced by the inland properties and human factors, would be all the possible reasons to explain the large uncertainty in the R_n_AVHRR_est in the coastal areas. Regarding to the high latitude oceans, it is generally accepted that large challenges exist for accurately retrieving the ocean surface radiation fluxes in high latitude oceans because of the complex interactions among the atmosphere, the ocean and the sea ice as point by Chaudhuri *et al*. [73]. Therefore, more cautions should be paid in these special regions.

Two site examples were presented in Fig. 8. The two sites were from the PIRATA and OceanSITES networks. And, the corresponding time series in R_n_JOFURO3 were also shown. In these two plots, the R_n_AVHRR_est captured the temporal variations in R_n_JOFURO3 very well, but both had the tendency to underestimate and overestimate the ocean surface R_n during the peak and valley periods, which agreed with Fig. 6.

In summary, the new developed downscaling models worked well for most sea areas, but the estimation errors increased over the costal and high latitude ocean areas.

A. Downscaled Ocean Surface R_n Mapping

In order to reduce the uncertainties and remove the prediction bias in R_n_AVHRR_est, a residual correction method based on the original R_n_JOFURO3 was conducted and generated the final ocean surface R_n estimations, namely R_n_AVHRR. For better illustration, one example was presented in Fig. 9. Figure 9 shows the comparison results in the bias between the R_n_AVHRR_est and R_n_AVHRR to the R_n_JOFURO3 at site TAO_01 (0 °, 95 °W), the red line in the plots represented the relative difference ratio. It was seen that the residual corrected R_n_AVHRR was more closer to the original R_n_JOFURO3

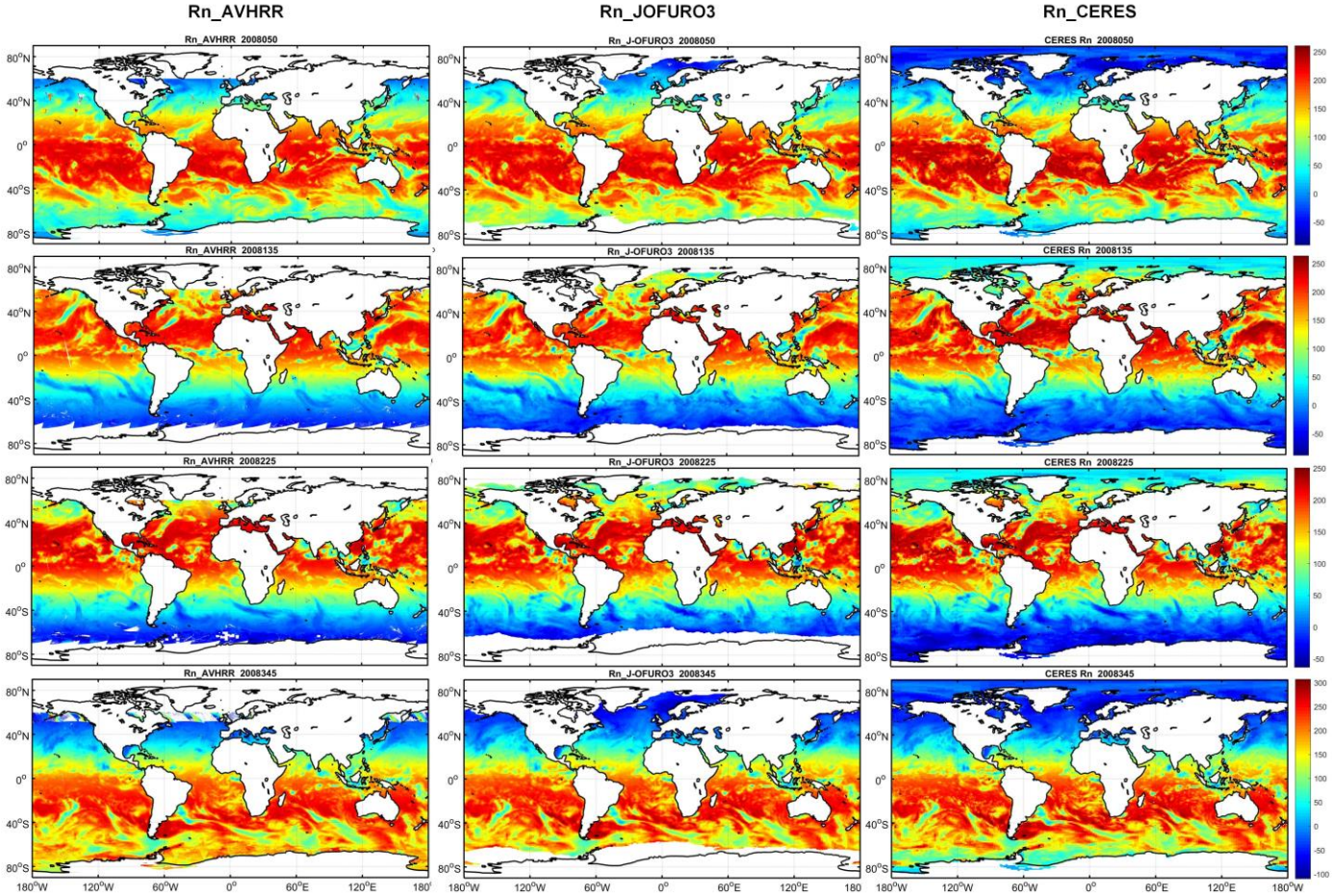

Fig. 12. Spatial explicit of R_n_AVHRR (0.05 °), R_n_JOFUR3 (0.25 °), and R_n_CERES (1 °) on the doy of 50, 135, 225 and 345 in 2008 from top to bottom. White color represents the missing data.

since the relative difference ratio was almost less than 5% (Fig. 9b), which illustrated that the post-processing step was incorporated necessarily in this study. However, the large residuals with relative differences being larger than 10% after residual correction are hardly to be corrected well, and these large residuals may be caused by the resampling operation in residual correction.

The quality of the maps of R_n_AVHRR was further assessed by visual comparison with the direct downscaled result 0.05 ° R_n_AVHRR_est, the 0.25 ° R_n_JOFURO3, the 0.75 ° ocean surface R_n from ERA-Interim (R_n_ERA-Interim), and the 1 ° ocean surface R_n from CERES (R_n_CERES) in two selected areas (Fig. 10). The study area A is a low latitude open sea located in the eastern Asia (Lat: 5 ° N ~ 20 °N, Lon: 135 °E ~ 140 °E), and the study area B is a high latitude ocean to the south of Greenland (Lat: 50 ° N ~ 60 °N, Lon: 35 °W ~ 45 °W). R_n_AVHRR_est and R_n_AVHRR maps reproduced much of the ocean surface R_n variation in the referenced three maps (R_n_JOFURO3, R_n_ERA-Interim, R_n_CERES) for both study areas, and similarly enhanced visual information in comparison to the original R_n_JOFURO3, but R_n_AVHRR map was more smooth than R_n_AVHRR_est, especially the areas with mosaics. Hence, it illustrated that the residual correction was helpful for global ocean surface R_n mapping. However, some areas cannot be downscaled (white color in the figures) because of the missing AVH021C data. The histograms of the differences between the R_n_AVHRR_est or R_n_AVHRR and the R_n_JOFURO3 within the two study areas were also examined and presented in Fig. 10. The results also proved that the differences were decreased after residual correction (Fig. 10a and Fig.10b).

Figure 11 displayed the comparison results of the variations in monthly ocean surface R_n from 2002 to 2013 for five different datasets and the buoy observations. Generally, the polylines of the R_n_AVHRR_est, R_n_AVHRR, R_n_CERES and R_n_JOFURO3 were closer to the buoy observations than R_n_ERA-Interim, and R_n_JOFURO3 and R_n_AVHRR fit the best with the buoy observations all over the year, while R_n_ERA-Interim presented an obvious underestimation from January to Septemper and overestimation after October. The residual correction nearly made R_n_AVHRR the same as R_n_JOFURO3. Specifically, the differences between R_n_AVHRR_est and R_n_CERES and the observations were increased mainly during the summer time (May to Sep.), which indicated that the dramatic air-sea interaction (dynamical adjustments and thermodynamic feedbacks) in this period would lead to a complex cloud environment and, therefore, more uncertainties would exist in ocean surface radiative components estimation. Among these data, only R_n_CERES has an obvious overestimation. This is most likely because CERES SYN1deg_Ed 4A cloud product underestimate the low-level clouds (11.8% and 20.9% for day and night) over the sun-glint

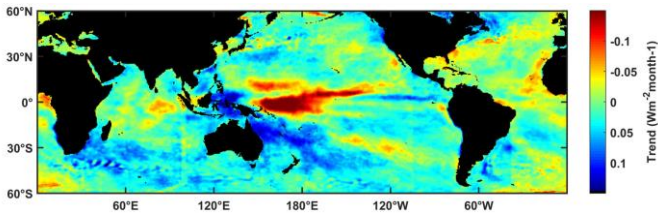

Fig. 13. Trend of deseasonalized monthly ocean surface R_n anomalies from 2002 to 2013 based on R_n_AVHRR.

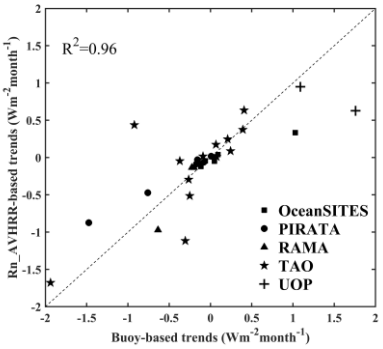

Fig. 14. Linear trends of the mean monthly R_n series obtained using the 40 R_n_AVHRR and buoy-based series over oceans during the period 2002-2013.

ocean and the polar region for both daytime and nighttime, though the CERES_Ed4A cloud property retrieval algorithms have improved significantly [74]. Due to overestimation of surface incident shortwave radiation [75], CI index calculated from CERES TOA and surface incident shortwave radiation presented an underestimation, which means a lower atmospheric transmission or a more turbid atmosphere. So an underestimation of R_n_AVHRR_est during the summer time was presented. Overall, it has demonstrated that the accuracy of R_n_JOFURO3 was satisfactory, and R_n_AVHRR improved spatial resolution and also kept its accuracy.

Fig. 12 showed the comparison of the global ocean surface R_n in R_n_AVHRR, R_n_JOFURO3, and R_n_CERES on the random selected dates in four seasons in 2008 (doy = 50, 135, 225 and 334). The spatial variations explicit in ocean surface R_n from the three datasets in the four plots seasons were very similar. It can be seen that the high R_n moving north from spring to summer and then south from autumn to winter, and the high R_n values in CERES were a little bit larger (the red color was darker) than R_n_AVHRR and R_n_JOFURO3. To be specific, the three maps (three panels in the first row, doy=50) were in March and most R_n was high over tropical oceans. This is due to the fact that the sun crosses the equator in March, that is, the sun is higher on the equator at noon, which eventually increases the daily amount of solar radiation reaching the surface so that R_n increases subsequently. Moreover, the atmosphere tends to be more stabilized because heating of the low stratosphere provides a more stable lid to the troposphere, which hinders atmosphere convection [76, 77]. In June (three panels in the second row, doy=135), the R_n increases with the sun moving to the Northern Hemisphere because the amount of solar radiation reaching Northern Hemisphere is increased dramatically. When the sun crosses the equator again by September (three panels in the third row, doy=225), the spatial variability and intensity of R_n decreases compared with that in summer in the Northern

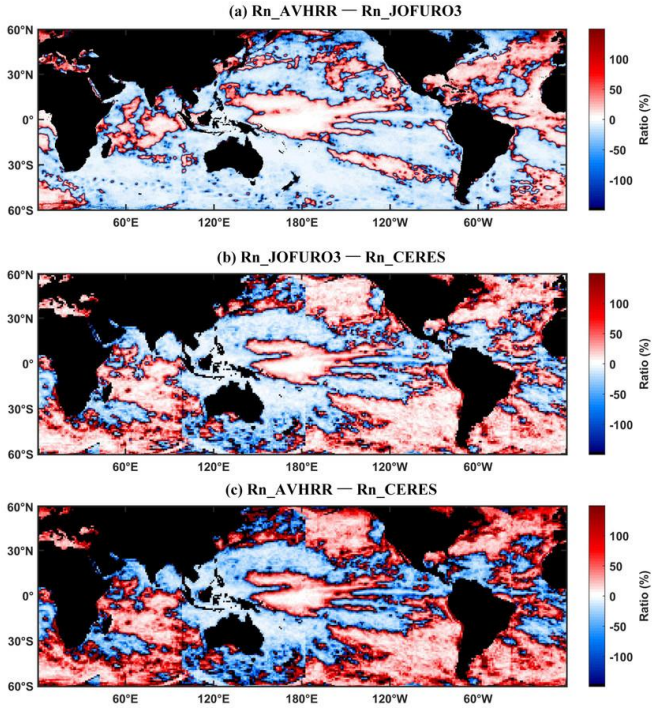

Fig. 15. (a) the ratio of the standard deviation of 0.05 °×0.05 ° R_n_AVHRR trend within 0.25 °×0.25 ° grid and the co-located R_n_JOFURO3 trend; (b) the ratio of the standard deviation of 0.25 °×0.25 ° R_n_JOFURO3 trend within 1 °×1 ° grid and the co-located R_n_CERES trend; (c) the ratio of the standard deviation of 0.05 °×0.05 ° R_n_AVHRR trend within 1 °×1 ° grid and the co-located R_n_CERES trend. All datasets cover same period from 2002 to 2013.

Hemisphere. It results from increased solar radiation in the Southern Hemisphere and decreased solar raidation in the Northern Hemisphere, and then R_n intensity changes subsequently. In December (three panels in the last ro, doy=334), the R_n intensity in the Southern Hemisphere becomes higher than that in the Northern Hemisphere when the sun moves to the Southern Hemisphere, which is opposite to that observed in June. It is noted that the missing areas (white color) in R_n_AVHRR was larger than R_n_JOFURO3. For one reason, the downscaling models cannot work in the polar region because of the limitation of the samples (ice-free), and the lacking of the AVH021C data was the other one.

B. Spatiotemporal Analysis of R_n_AVHRR

The long-time R_n_AVHRR series from 2002 to 2013 was generated, and then the trend of deseasonalized monthly ocean surface R_n anomalies was calculated below latitude 60° oceans. Results were given in Fig. 13. It was observed that the overall trend in ocean surface R_n during the study period was downward. Specifically, ocean surface R_n significantly decreased (blue color) in the central Pacific near Austria, while it significantly increased in the central and eastern Pacific near the equator (red color). The spatial distribution of ocean surface R_n trends was consistent with the study of Tan [77] that a positive trend of Photosynthetically active radiation (PAR) was revealed at west of Central America around 15 ℃N and west of South America around 20 ℃S and in the central Pacific around latitude 5 ℃S.

To further prove the reliability of trend of R_n_AVHRR, a comparison of trends of the mean monthly R_n series obtained using R_n_AVHRR and buoy observations series at 40 buoy locations was presented in Fig. 14. The trends for the mean

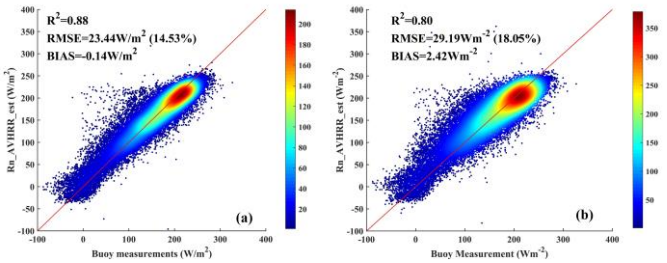

Fig. 16. Daily R_n_AVHRR_est validation results for (a) with CI and (b) without CI under all-sky condition.

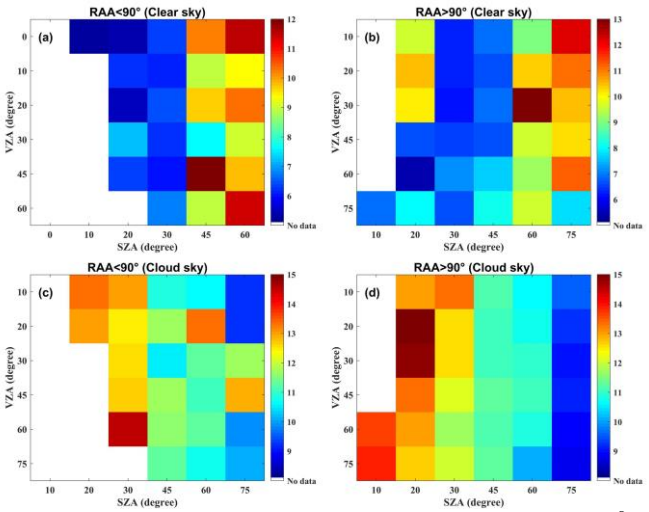

Fig. 17. Fitting RMSE of the ocean surface R_n downscaling models (W/m^2) in each angular bin for (a) RAA < 90 ° under clear-sky, (b) RAA > 90 ° under clear-sky, (c) RAA < 90 ° under cloud sky, and (d) RAA > 90 ° under cloud sky.

monthly R_n series of the 40 R_n_AVHRR and buoy-based series showed an agreement in the signs and values throughout the study period 2002-2013, which proved the consistency between R_n_AVHRR and buoy observations and increased the confidence of the spatial distribution of trends in Fig. 13. After analysis, the abnormal data points with a large magnitude of trend was caused by the series missing of buoy observations series.

The AVHRR TOA data applied in this study not only downscaled the R_n_JOFURO3, but also increased the information of trend change of deseasonalized monthly average R_n. Hence, the temporal change information that different from the orignial R_n_JOFURO3 was explored. The standard deviation of 0.05 °×0.05 ° R_n_AVHRR trend within each corresponding 0.25 °×0.25 ° coarse grid was compared with the co-located R_n_JOFURO3 trend (Fig. 15a). The ratios were also presented between R_n_JOFURO3 and R_n_CERES (Fig.15b) as well as between R_n_AVHRR and R_n_CERES in the same way (Fig. 15c). The larger the ratio in Fig. 15a, the more information of temporal change provided by R_n_AVHRR compared to R_n_JOFURO3. On the other hand, R_n_AVHRR can also be proved to illustrate more spatial details of trend variations compared to R_n_JOFURO3 when we use trend information of R_n_CERES as a reference (Fig. 15b and c). Based on Fig. 15a, it showed that spatial variability of the R_n_AVHRR trend was greater than that of R_n_JOFURO3 at several ocean regions, including central tropical Pacific (warming pool), Atlantic and

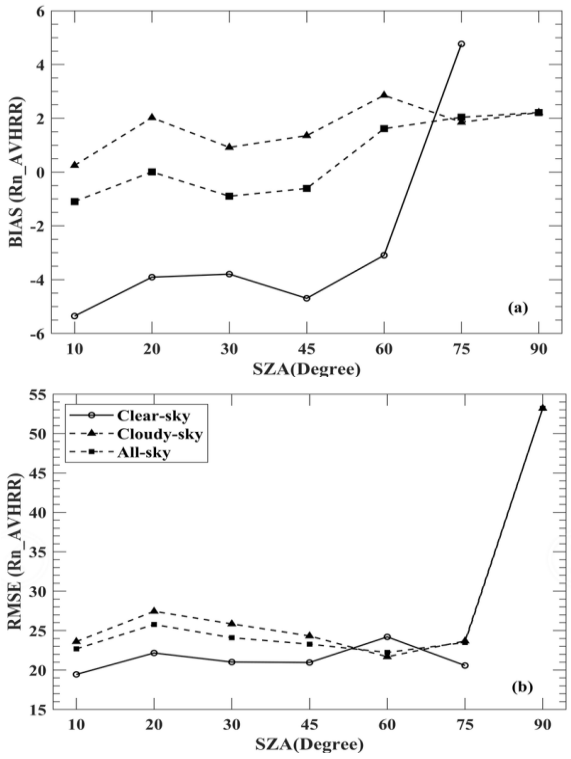

Fig. 18. The validation bias (W·m^{-2}) (a) and RMSE (W·m^{-2}) (b) against the buoy observations for different SZA in clear-sky, cloudy-sky and all-sky.

Equatorial Eastern Indian Ocean (EIO) and meanwhile, these ocean regions have R_n with a more dramatic variation of trend. Because of El Niño-Southern Oscillation (ENSO) event, many studies have been conducted to investigate the impact of ENSO on ocean climate changes based on surface radiative fluxes and meteorological variables over the tropical Pacific using satellite observations and atmospheric reanalysis [78, 79]. Meanwhile, incoming shortwave and absorb outgoing longwave radiation were also frequently used to study Indian Summer Monsoon (ISM) over EIO since radiation budget has a great impact on *SST* [80]. In terms of these hotspot ocean regions, R_n_AVHRR may be an ideal data source for studying long term ocean climate changes and local disaster events due to its high spatial resolution, high accuracy and reasonable temporal trend.

V. UNCERTAINTIES ANALYSIS

To downscale the ocean surface R_n in J-OFURO3, a series of new downscaling models were built by using the AVH021C data in this study, and the validation results proved the ability of these models. However, as mentioned above, the uncertainties were still large in some regions. Therefore, the reasons were explored and discussed in this section.

A. The Effect of CI

CI is usually used to represent the daily average atmospheric condition. In this study, the downscaling models were built based on the AVHRR TOA instantaneous observations, which can only provide the instantaneous atmospheric condition. However, previous studies [53-55] usually assumed the instantaneous atmospheric condition was invariant during a day, which was pointed out unreasonable in Wang's study [81].

Therefore, CI was introduced in these downscaling models. To better understanding the effect of CI, the estimation validation results with and without introducing CI were shown in Fig. 16. A large increase in RMSE and bias could be observed from 23.44 to 29.19 $W \cdot m^{-2}$ and -0.14 to 2.42 $W \cdot m^{-2}$, respectively. In one word, it is very effective to improve the validation accuracy by adding CI to our downscaling models.

B. Viewing Geometry

The impacts of geometric information (SZA, VZA, and RAA) on the downscaling models were also analyzed. As stated in Section 3.2, each downscaling model was built using the training data in each angular bin (see Fig. 4), hence, the variations in the fitting accuracies of these models represented as the RMSE ($W \cdot m^{-2}$) with geometric information was examined. The fitting accuracies were divided by the combination of RAA (less or larger than 90 °) and sky condition (clear or cloudy-sky), and the results were shown in Fig. 17. It should be noted that the blank grids in the figure because of the few samples in these cases. Generally speaking, no significant difference was found between the smaller (< 90 °) and larger (> 90 °) RAA under the same sky condition, but the RMSE values ranged from 5 to 12 $W \cdot m^{-2}$ under clear-sky and from 8 to 15 $W \cdot m^{-2}$ under cloudy-sky, respectively. Specifically, for clear-sky, the model prediction errors were the smallest when SZA and VZA both were less than 45 °, and increased when the SZA increased up to 60 °(Fig.18a and b); for cloudy-sky the case was opposite that the prediction errors were smaller when SZA was larger than 45 ° (Fig.17c and d). Therefore, it could be concluded that the influence of SZA on model performance is much larger than VZA and RAA.

Besides, the variations in the validation accuracy (represented by bias and RMSE) with SZA under clear-, cloudy-, and all-sky conditions were also examined in Fig. 18. It was indicated that downscaling models worked worse when SZA larger than 45 °under clear-sky but smaller than 60 °under cloudy-sky, which was agree well with Fig. 17. Moreover, it was also found that the bias was overly positive for cloudy-sky and negative for clear-sky but with a sharp increase to positive when SZA was larger than 60 ° (Fig. 18a). According to the statistic results, the ocean surface R_n values were most less than 0 $W \cdot m^{-2}$ when SZA was larger than 60 °, which was also agree well with the result presented in Fig. 6 that overestimation appeared when ocean surface R_n was very small. The uncertainties increased when SZA was large under cloudy-sky condition could be explained with three reasons. For first one, the clouds and the large SZAs would block or reduce the surface information reaching to the satellite, and for the second one, the uncertainties of the original R_n_JOFURO3 were large, and the third one, few samples could be collected for modeling in these cases (see Fig.4), which made the performances of these models poor.

C. Others

As described above, the accuracy of R_n_AVHRR_est in the coastal areas was worse than that in the open oceans, which might be caused by the large uncertainty in R_n_JOFURO3 and its relative coarse spatial resolution. One sample in R_n_JOFURO3 at coastal areas were usually mixed with land surface and ocean at 0.25°, but it was still taken as a pure pixel for modeling. Even some techniques were implemented in J-OFURO3 to improve accuracy of gridded products over the sea near the land-sea boundaries [82], it seems more efforts still needs to be done. Hence, other information, such as the reanalysis products, other satellite observations, and so on, could be taken into account in the downscaling models in the future to improve the estimations in the coastal areas or high latitude oceans.

Overall, the factors to make the performance of the downscaling models poor in some special cases are objective and should be addressed in future studies.

VI. CONCLUSIONS

Ocean surface net radiation R_n at high spatial resolution is required for regional or local ocean climate and air-sea interaction researches. However, the spatial resolutions of most available ocean surface R_n products are very coarse (> 1 °). To our best knowledge, the daily ocean surface R_n from the satellite-based J-OFURO3 product has been reported to be one of the best datasets [14], but its spatial resolution is still as coarse as 0.25 °. The downscaling method was used to enhance the spatial resolution of a parameter without losing its original accuracy, and it was successfully utilized in various applications (i.e., soil moisture, land surface temperature). Therefore, a downscaling scheme was developed in this study to obtain the daily ocean surface R_n with a high spatial resolution from J-OFURO3.

By considering the advantages of satellite data, the AVHRR TOA observations (AVH021C) was used for its high spatial resolution (0.05 °), long time-span (1978-present) and global coverage. In this study, the downscaling scheme consists of the downscaling statistical models and residual correction to the model estimates. First of all, a series of angle-dependent downscaling statistical models were established between the daily ocean surface R_n in J-OFURO3 and the corresponding aggregated AVHRR TOA data and other ancillary information by assuming the relationship was the same for each AVHRR pixel. Afterwards, the residual correction was conducted to the model estimates (R_n_AVHRR_est) based on the original data (R_n_JOFURO3) to reduce the prediction biases. Finally, the downscaling scheme was applied to generate a time series daily ocean surface R_n dataset at 0.05 °resolution from 2002 to 2013 (R_n_AVHRR).

After validating against the measurements from 57 global buoy sites, it was shown that the accuracy of R_n_AVHRR_est with an R^2 of 0.88, an RMSE of 23.44 $W \cdot m^{-2}$ (14.53%), and a bias of -0.14 $W \cdot m^{-2}$ under all-sky condition, which was very close to the original R_n_JOFURO3. Further analysis indicated that the spatio-temporal variations in R_n_AVHRR_est was also consistent with R_n_JOFURO3, hence, it was demonstrated that the performances of these new developed downscaling models were satisfactory and generally robust. For comprehensive validation, the generated dataset R_n_AVHRR was inter-compared with the CERES SYN1deg_Ed4A and the reanalysis ERA-Interim products. The inter-comparison results indicated that R_n_AVHRR not only has a very similar spatial explicit with other products, but also could provide more detailed information especially for those hotspots in the current local

ocean climate events and studies, which could help us further understand the ocean climate change.

However, the limitations cannot be ignored: (1) these downscaling statistical models performed poor as long as the SZA was large, which was possibly due to the limited amount of samples for model training; (2) the information contained in CI index was limited (only accounted for radiation variation in the shortwave range) though it was usually introduced to represent the daily average atmospheric condition; (3) the coastal mixed pixels have larger uncertainties, and (4) the missing data in the R_n_AVHRR was due to the unavailability of AVH02C1 data, which was primary designed for the land applications [83, 84]. Moreover, the uncertainties caused by the AVHRR cloud mask were needed to be taken into account in the future. More efforts would be taken to improve the performance of the downscaling models and the quality of R_n_AVHRR dataset in the future work.

ACKNOWLEDGMENT

The authors would like to thank LTDR for providing AVHRR data, NASA/GSFC for CERES data, J-OFURO for J-OFURO3 flux data and ECMWF for ERA-Interim data. We also thank PIRATA, RAMA, TAO, UOP, OceanSITES, CN-NADC networks for offering the filed measurements of flux variables. We are grateful for all the anonymous reviewers for their constructive comments that greatly helped improve the quality of this paper.

REFERENCES

[1] K. E. Trenberth, J. T. Fasullo, and J. Kiehl, "Earth's global energy budget," *Bulletin of the American Meteorological Society*, vol. 90, no. 3, pp. 311-324, 2009.

[2] G. O. Löf, J. A. Duffie, and C. O. Smith, "World distribution of solar radiation," *Solar Energy*, vol. 10, no. 1, pp. 27-37, 1966.

[3] M. R. Lewis, M.-E. Carr, G. C. Feldman, W. Esaias, and C. McClain, "Influence of penetrating solar radiation on the heat budget of the equatorial Pacific Ocean," *Nature*, vol. 347, no. 6293, p. 543, 1990.

[4] J. C. Chan, "Tropical cyclone activity in the northwest Pacific in relation to the El Niño/Southern Oscillation phenomenon," *Monthly Weather Review*, vol. 113, no. 4, pp. 599-606, 1985.

[5] P.-S. Chu and J.-B. Wang, "Recent climate change in the tropical western Pacific and Indian Ocean regions as detected by outgoing longwave radiation records," *Journal of Climate*, vol. 10, no. 4, pp. 636-646, 1997.

[6] Z. Ling, F. Sielmann, K. Fraedrich, and X. Zhi, "Atmospheric response to Indian Ocean Dipole forcing: changes of Southeast China winter precipitation under global warming," *Climate Dynamics*, vol. 48, no. 5-6, pp. 1-16, 2016.

[7] C. W. Fairall, E. F. Bradley, J. E. Hare, A. A. Grachev, and J. B. Edson, "Bulk Parameterization of Air Sea Fluxes: Updates and Verification for the COARE Algorithm," *Journal of Climate*, vol. 16, no. 4, pp. 571-591, 2003.

[8] C. W. Fairall, E. F. Bradley, D. P. Rogers, J. B. Edson, and G. S. Young, "Bulk parameterization of air-sea fluxes for tropical ocean-global atmosphere coupled - ocean atmosphere response experiment," *Journal of Geophysical Research: Oceans*, vol. 101, no. C2, pp. 3747-3764, 1996.

[9] S. A. Josey, D. Oakley, and R. W. Pascal, "On estimating the atmospheric longwave flux at the ocean surface from ship meteorological reports," *Journal of Geophysical Research Oceans*, vol. 102, no. C13, pp. 27961-27972, 1997.

[10] F. Bignami, Marullo, R. Santoleri, and M. E. Schiano, "Longwave radiation budget in the Mediterranean Sea," *Journal of Geophysical Research Oceans*, vol. 100, no. C2, pp. 2501–2514, 1995.

[11] C. Ladd and N. A. Bond, "Evaluation of the NCEP/NCAR reanalysis in the NE Pacific and the Bering Sea," *Journal of Geophysical Research Oceans*, vol. 107, no. C10, pp. 22-1-22-9, 2002.

[12] M. Valdivieso *et al.*, "An assessment of air–sea heat fluxes from ocean and coupled reanalyses," *Climate Dynamics*, vol. 49, no. 3, pp. 983-1008, 2017.

[13] Y. Cao, S. Liang, X. Chen, and T. He, "Assessment of sea ice albedo radiative forcing and feedback over the Northern Hemisphere from 1982 to 2009 using satellite and reanalysis data," *Journal of Climate*, vol. 28, no. 3, pp. 1248-1259, 2015.

[14] B. Jiang and X. X. Li, "Inter-comparison and evaluation of ten sea surface net radiation estimates," *Journal of Geophysical Research: Oceans*, 2019.

[15] M. Kubota, N. Iwabe, M. F. Cronin, and H. Tomita, "Surface heat fluxes from the NCEP/NCAR and NCEP/DOE reanalyses at the Kuroshio Extension Observatory buoy site," *Journal of Geophysical Research Oceans*, vol. 113, no. C2, pp. -, 2008.

[16] MOORE, W. K. G., RENFREW, and A. I., *An assessment of the surface turbulent heat fluxes from the NCEP-NCAR reanalysis over the western boundary currents*. 2002.

[17] H. Tomita, T. Hihara, S. i. Kako, M. Kubota, and K. Kutsuwada, "An introduction to J-OFURO3, a third-generation Japanese ocean flux data set using remote-sensing observations," *Journal of Oceanography*, vol. 75, no. 2, pp. 171-194, 2019.

[18] H. F. Diaz, M. P. Hoerling, and J. K. Eischeid, "ENSO variability, teleconnections and climate change," *International Journal of Climatology*, vol. 21, no. 15, pp. 1845-1862, 2010.

[19] J. E. Kay, C. Wall, V. Yettella, B. Medeiros, and C. Bitz, "Global climate impacts of fixing the Southern Ocean shortwave radiation bias in the Community Earth System Model (CESM)," in *Agu Fall Meeting*, 2015.

[20] B. van de Schootbrugge *et al.*, "Early Jurassic climate change and the radiation of organic-walled phytoplankton in the Tethys Ocean," *Paleobiology*, vol. 31, no. 1, pp. 73-97, 2005.

[21] J. Peng, A. Loew, O. Merlin, and N. E. C. Verhoest, "A review of spatial downscaling of satellite remotely sensed soil moisture," *Reviews of Geophysics*, vol. 55, 2017.

[22] S. Park, S. Park, J. Im, J. Rhee, J. Shin, and J. Park, "Downscaling GLDAS Soil Moisture Data in East Asia through Fusion of Multi-Sensors by Optimizing Modified Regression Trees," *Water*, vol. 9, no. 5, p. 332, 2017.

[23] Y. Yang, C. Cao, X. Pan, X. Li, and X. Zhu, "Downscaling Land Surface Temperature in an Arid Area by Using Multiple Remote Sensing Indices with Random Forest Regression," *Remote Sensing*, vol. 9, no. 8, p. 789, 2017.

[24] M. Mahour, V. Tolpekin, A. Stein, and A. Sharifi, "A comparison of two downscaling procedures to increase the spatial resolution of mapping actual evapotranspiration," *Isprs Journal of Photogrammetry & Remote Sensing*, vol. 126, pp. 56-67, 2017.

[25] B. Hewitson and R. Crane, "Consensus between GCM climate change projections with empirical downscaling: precipitation downscaling over South Africa," *International Journal of Climatology*, vol. 26, no. 10, pp. 1315-1337, 2006.

[26] M. Piles *et al.*, "A Downscaling Approach for SMOS Land Observations: Evaluation of High-Resolution Soil Moisture Maps Over the Iberian Peninsula," *IEEE Journal of Selected Topics in Applied Earth Observations & Remote Sensing*, vol. 7, no. 9, pp. 3845-3857, 2014.

[27] C. Hutengs and M. Vohland, "Downscaling land surface temperatures at regional scales with random forest regression," *Remote Sensing of Environment*, vol. 178, pp. 127-141, 2016.

[28] A. P. Cracknell, *Advanced very high resolution radiometer AVHRR*. CRC Press, 1997.

[29] Z. Song, S. Liang, D. Wang, Y. Zhou, and A. Jia, "Long-term record of top-of-atmosphere albedo over land generated from AVHRR data," *Remote sensing of environment*, vol. 211, pp. 71-88, 2018.

[30] K. P. Bowman, A. B. Phillips, and G. R. North, "Comparison of TRMM rainfall retrievals with rain gauge data from the TAO/TRITON buoy array," *Geophysical Research Letters*, vol. 30, no. 14, 2003.

[31] B. Bourlès *et al.*, "The PIRATA program: History, accomplishments, and future directions," *Bulletin of the American Meteorological Society*, vol. 89, no. 8, pp. 1111-1126, 2008.

[32] M. J. McPhaden *et al.*, "RAMA: the research moored array for African–Asian–Australian monsoon analysis and prediction,"

Bulletin of the American Meteorological Society, vol. 90, no. 4, pp. 459-480, 2009.

[33] K. Steele, E. Burdette, and A. Trampus, "A system for the routine measurement of directional wave spectra from large discus buoys," in *OCEANS'78*, 1978, pp. 614-621: IEEE.

[34] W. Weiqiang, C. Liqi, Y. Xulin, and H. Xuanbao, "Investigations on distributions and fluxes of sea-air CO2 of the expedition areas in the Arctic Ocean," *Science in China. Series D: Earth sciences*, vol. 46, no. 6, pp. 569-579, 2003.

[35] Y. Feng, Q. Liu, Y. Qu, and S. Liang, "Estimation of the ocean water albedo from remote sensing and meteorological reanalysis data," *IEEE Transactions on Geoscience and Remote Sensing*, vol. 54, no. 2, pp. 850-868, 2015.

[36] J. Cheng, X. Cheng, X. Meng, and G. Zhou, "A Monte Carlo Emissivity Model for Wind-Roughened Sea Surface," *Sensors*, vol. 19, no. 9, p. 2166, 2019.

[37] D. Halpern *et al.*, "The tropical ocean-global atmosphere (TOGA) observing system: a decade of progress," *J Geophys Res*, vol. 103, no. 14, p. 16914240, 1998.

[38] Pukelsheim and Friedrich, "The Three Sigma Rule," *American Statistician*, vol. 48, no. 2, pp. 88-91.

[39] J. Pedelty *et al.*, "Generating a long-term land data record from the AVHRR and MODIS instruments," in *2007 IEEE International Geoscience and Remote Sensing Symposium*, 2007, pp. 1021-1025: IEEE.

[40] E. Vermote and Y. Kaufman, "Absolute calibration of AVHRR visible and near-infrared channels using ocean and cloud views," *International Journal of Remote Sensing*, vol. 16, no. 13, pp. 2317-2340, 1995.

[41] R. Evans, K. Casey, and P. Cornillon, "Transition of AVHRR SST Pathfinder to Version 6, continued evolution of a CDR," 2010.

[42] B. Franch *et al.*, "A 30+ year AVHRR land surface reflectance climate data record and its application to wheat yield monitoring," *Remote Sensing*, vol. 9, no. 3, p. 296, 2017.

[43] R. Pinker and J. Tarpley, "The relationship between the planetary and surface net radiation: An update," *Journal of Applied Meteorology*, vol. 27, no. 8, pp. 957-964, 1988.

[44] H. Tomita and T. Hihara, "J-OFURO3."

[45] W. Rossow and Y. C. Zhang, "Calculation of surface and top of atmosphere radiative fluxes from physical quantities based on ISCCP data sets: 2. Validation and first results," *Journal of Geophysical Research: Atmospheres*, vol. 100, no. D1, pp. 1167-1197, 1995.

[46] B. A. Wielicki, B. R. Barkstrom, E. F. Harrison, R. B. Lee III, G. L. Smith, and J. E. Cooper, "Clouds and the Earth's Radiant Energy System (CERES): An earth observing system experiment," *Bulletin of the American Meteorological Society*, vol. 77, no. 5, pp. 853-868, 1996.

[47] A. Jia, S. Liang, B. Jiang, X. Zhang, and G. Wang, "Comprehensive Assessment of Global Surface Net Radiation Products and Uncertainty Analysis," *Journal of Geophysical Research: Atmospheres*, 2017.

[48] S. Kato *et al.*, "Surface Irradiances Consistent with CERES-Derived Top-of-Atmosphere Shortwave and Longwave Irradiances," *Journal of Climate*, vol. 26, no. 9, pp. 2719-2740, 2013.

[49] D. P. Dee *et al.*, "The ERA‐Interim reanalysis: Configuration and performance of the data assimilation system," *Quarterly Journal of the royal meteorological society*, vol. 137, no. 656, pp. 553-597, 2011.

[50] M. Zygmuntowska, T. Mauritsen, J. Quaas, and L. Kaleschke, "Arctic Clouds and Surface Radiation–a critical comparison of satellite retrievals and the ERA-Interim reanalysis," *Atmospheric Chemistry and Physics*, vol. 12, no. 14, pp. 6667-6677, 2012.

[51] A. Boilley and L. Wald, "Comparison between meteorological re-analyses from ERA-Interim and MERRA and measurements of daily solar irradiation at surface," *Renewable Energy*, vol. 75, pp. 135-143, 2015.

[52] S. Kothe and B. Ahrens, "On the radiation budget in regional climate simulations for West Africa," *Journal of Geophysical Research: Atmospheres*, vol. 115, no. D23, 2010.

[53] D. Wang, S. Liang, T. He, and Q. Shi, "Estimation of Daily Surface Shortwave Net Radiation From the Combined MODIS Data," *IEEE Transactions on Geoscience & Remote Sensing*, vol. 53, no. 10, pp. 5519-5529, 2015.

[54] D. Wang and S. Liang, "Estimating top-of-atmosphere daily reflected shortwave radiation flux over land from MODIS data," *IEEE Transactions on Geoscience and Remote Sensing*, vol. 55, no. 7, pp. 4022-4031, 2017.

[55] D. Wang, S. Liang, T. He, Y. Cao, and B. Jiang, "Surface shortwave net radiation estimation from fengyun-3 mersi data," *Remote sensing*, vol. 7, no. 5, pp. 6224-6239, 2015.

[56] Y. Z. Wang and B. Jiang, "Surface Shortwave Net Radiation Estimation from Landsat TM/ETM+ data using four machine learning algorithms," *Remote Sensing*, 2019.

[57] B. Jiang *et al.*, "GLASS daytime all-wave net radiation product: Algorithm development and preliminary validation," *Remote Sensing*, vol. 8, no. 3, p. 222, 2016.

[58] M. G. Iziomon, H. Mayer, and A. Matzarakis, "Downward atmospheric longwave irradiance under clear and cloudy skies: Measurement and parameterization," *Journal of Atmospheric and Solar-Terrestrial Physics*, vol. 65, no. 10, pp. 1107-1116, 2003.

[59] N. Hatzianastassiou *et al.*, "Long-term global distribution of earth's shortwave radiation budget at the top of atmosphere," *Atmospheric Chemistry and Physics*, vol. 4, no. 5, pp. 1217-1235, 2004.

[60] A. Jia, B. Jiang, S. Liang, X. Zhang, and H. Ma, "Validation and Spatiotemporal Analysis of CERES Surface Net Radiation Product," *remote sensing*, 2016.

[61] V. Hodge and J. Austin, "A Survey of Outlier Detection Methodologies," *Artificial Intelligence Review*, vol. 22, no. 2, pp. 85-126, 2004.

[62] N. C. Schwertman, M. A. Owens, and R. Adnan, "A simple more general boxplot method for identifying outliers," *Computational statistics & data analysis*, vol. 47, no. 1, pp. 165-174, 2004.

[63] Y. Huang, "Advances in Artificial Neural Networks – Methodological Development and Application," *Algorithms*, vol. 2, no. 3, pp. 973-1007, 2009.

[64] K. Suzuki, *Artificial neural networks: methodological advances and biomedical applications*. BoD–Books on Demand, 2011.

[65] Y. Wang and H. Xu, "Spectral characterization of scanner based on PCA and BP ANN," *Chinese Optics Letters*, vol. 3, no. 12, pp. 725-728, 2005.

[66] G. Caocci, R. Baccoli, and G. La Nasa, "The usefulness of artificial neural networks in predicting the outcome of hematopoietic stem cell transplantation," *Edited by Kenji Suzuki*, p. 217, 2011.

[67] W. P. Kustas, J. M. Norman, M. C. Anderson, and A. N. French, "Estimating subpixel surface temperatures and energy fluxes from the vegetation index–radiometric temperature relationship," *Remote sensing of environment*, vol. 85, no. 4, pp. 429-440, 2003.

[68] F. Gao, W. Kustas, and M. Anderson, "A data mining approach for sharpening thermal satellite imagery over land," *Remote Sensing*, vol. 4, no. 11, pp. 3287-3319, 2012.

[69] X. Chen, W. Li, J. Chen, Y. Rao, and Y. Yamaguchi, "A combination of TsHARP and thin plate spline interpolation for spatial sharpening of thermal imagery," *Remote Sensing*, vol. 6, no. 4, pp. 2845-2863, 2014.

[70] C. Hutengs and M. Vohland, "Downscaling land surface temperatures at regional scales with random forest regression," *Remote Sensing of Environment*, vol. 178, pp. 127-141.

[71] H. Tomita, T. Hihara, S. Kako, M. Kubota, and K. Kutsuwada, "An introduction to J-OFURO3, a third-generation Japanese ocean flux data set using remote-sensing observations," *Journal of Oceanography*, vol. 75, no. 2, pp. 171-194, 2019.

[72] A. B. Kara, A. J. Wallcraft, C. N. Barron, H. E. Hurlburt, and M. A. Bourassa, "Accuracy of 10 m winds from satellites and NWP products near land‐sea boundaries," *Journal of Geophysical Research*, vol. 113, 2008.

[73] A. H. Chaudhuri, R. M. Ponte, and A. T. Nguyen, "A Comparison of Atmospheric Reanalysis Products for the Arctic Ocean and Implications for Uncertainties in Air–Sea Fluxes," *Journal of Climate*, vol. 27, no. 14, pp. 5411-5421, 2014.

[74] B. Xi, S. Qiu, X. Dong, W. L. Smith Jr, P. Minnis, and S. Sun-Mack, "Evaluation of CERES-MODIS Ed4 Cloud Macrophysical Properties using 11-yr ARM Ground-based Observations over the Arctic," in *AGU Fall Meeting Abstracts*, 2018.

[75] X. Zhang, S. Liang, M. Wild, and B. Jiang, "Analysis of surface incident shortwave radiation from four satellite products," *Remote Sensing of Environment*, vol. 165, pp. 186-202, 2015.

[76] J. Haigh, "Solar influences on Climate," *Grantham Institute for Climate Change*, 2011.
[77] J. Tan and R. Frouin, "Seasonal and Interannual Variability of Satellite-Derived Photosynthetically Available Radiation Over the Tropical Oceans," *Journal of Geophysical Research: Oceans*, vol. 124, no. 5, pp. 3073-3088, 2019.
[78] R. Pinker, S. Grodsky, B. Zhang, A. Busalacchi, and W. Chen, "ENSO impact on surface radiative fluxes as observed from space," *Journal of Geophysical Research: Oceans*, vol. 122, no. 10, pp. 7880-7896, 2017.
[79] K. Pavlakis, N. Hatzianastassiou, C. Matsoukas, A. Fotiadi, and I. Vardavas, "ENSO surface shortwave radiation forcing over the tropical Pacific," *Atmospheric Chemistry and Physics*, vol. 8, no. 18, pp. 5565-5577, 2008.
[80] H. S. Chaudhari, A. Hazra, S. Pokhrel, C. Chakrabarty, S. K. Saha, and P. Sreenivas, "SST and OLR relationship during Indian summer monsoon: a coupled climate modelling perspective," *Meteorology and Atmospheric Physics*, vol. 130, no. 2, pp. 211-225, 2018.
[81] Y. Wang *et al.*, "Surface Shortwave Net Radiation Estimation from Landsat TM/ETM+ Data Using Four Machine Learning Algorithms," *Remote Sensing*, vol. 11, no. 23, p. 2847, 2019.
[82] A. B. Kara, A. J. Wallcraft, and H. E. Hurlburt, "A correction for land contamination of atmospheric variables near land–sea boundaries," *Journal of physical oceanography*, vol. 37, no. 4, pp. 803-818, 2007.
[83] M. Claverie, J. Matthews, E. Vermote, and C. Justice, "A 30+ year AVHRR LAI and FAPAR climate data record: Algorithm description and validation," *Remote Sensing*, vol. 8, no. 3, p. 263, 2016.
[84] C. J. Tucker *et al.*, "An extended AVHRR 8-km NDVI dataset compatible with MODIS and SPOT vegetation NDVI data," *International Journal of Remote Sensing*, vol. 26, no. 20, pp. 4485-4498, 2005.

Jianglei Xu is currently pursuing the M.S. degree in cartography and geographical information system with the State Key Laboratory of Remote Sensing Science, Faculty of Geographical Science, Beijing Normal University, Beijing, China.

His research interests include the estimation of ocean surface net radiation from satellite data.

Bo Jiang received the B.S. degree in mapping and surveying engineer from Central South University, Changsha, China, in 2006, and the M.E. degree in cartography and geographical information system and the Ph.D. degree from Beijing Normal University, Beijing, China, in 2009 and 2012, respectively.

From 2010 to 2012, she was a joint Ph.D. Student with the Department of Geographical Sciences, University of Maryland at College Park, College Park, MD, USA. She is currently with the Faculty of Geographical Science, Institute of Remote Sensing Science and Engineering, Beijing Normal University. Her research interests include net radiation estimation by using remote sensing data, time series analysis, assessing the impacts of the land cover change on the climate from various observations, and application of remote sensing products.

Shunlin Liang (M'94–F'13) received the Ph.D. degree from Boston University, Boston, MA, USA.

He is currently a Professor with the Department of Geographical Sciences, University of Maryland at College Park, College Park, MD, USA, and the State Key Laboratory of Remote Sensing Science, School of Geography, Beijing Normal University, Beijing, China. He has published over 220 peerreviewed journal papers, authored the book *Quantitative Remote Sensing of Land Surfaces* (Wiley, 2004), coauthored the book *Global LAnd Surface Satellite (GLASS) Products: Algorithms, Validation and Analysis* (Springer, 2013), edited the book *Advances in Land Remote Sensing: System, Modeling, Inversion and Application* (Springer, 2008), and coedited the books *Advanced Remote Sensing: Terrestrial Information Extraction and Applications* (Academic Press, 2012) and *Land Surface Observation, Modeling, Data Assimilation* (World Scientific, 2013). His research interests include the estimation of land surface variables from satellite data, earth's energy balance, and assessment of environmental impacts of vegetation changes.

Dr. Liang was an Associate Editor of the IEEE TRANSACTIONS ON GEOSCIENCE AND REMOTE SENSING and a guest editor of several remote sensing-related journals.

Xiuxia Li received the B.S. degree in mapping and surveying engineer in 2016 from the Institute of Remote Sensing and Digital Earth, Chinese Academy of Science, Beijing, China and the M.E. degree in mapping and surveying engineer from Nanjing TECH University in 2013. She is currently pursuing the Ph.D. degree with the Cartography and Geography Information System in Beijing Normal University.

Since 2018, she has been a visiting Ph.D. student with the University of Maryland, College Park, MD, USA. Her research interests include remote sensing image fusion, applications of remotely sensed data and machine learning.

Yezhe Wang received the M.S. degree in cartography and geographical information system with the State Key Laboratory of Remote Sensing Science, Faculty of Geographical Science, Beijing Normal University, Beijing, China, in 2009.

Her research interests include land surface radiation budgets retrieval from various remotely sensed data and land surface products validation.

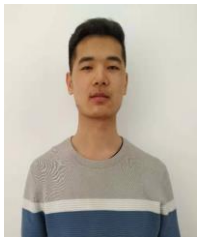

Jianghai Peng is currently pursuing the M.S. degree in cartography and geographical information system with the State Key Laboratory of Remote Sensing Science, Faculty of Geographical Science, Beijing Normal University, Beijing, China.

His research interests include the estimation of ocean surface net radiation from satellite data and meteorological data.

Hongkai Chen is currently pursuing the M.S. degree in cartography and geographical information system with the State Key Laboratory of Remote Sensing Science, Faculty of Geographical Science, Beijing Normal University, Beijing, China.

His research interests include the estimation of land surface net radiation from satellite data.

Hui Liang is currently pursuing the M.S. degree in photogrammetry and remote sensing with the State Key Laboratory of Remote Sensing Science, Faculty of Geographical Science, Beijing Normal University, Beijing, China**.**

Her research interests include the spatiotemporal fusion of ocean surface net radiation from satellite data.

Shaopeng Li is currently pursuing the M.S. degree in photogrammetry and remote sensing with the State Key Laboratory of Remote Sensing Science, Faculty of Geographical Science, Beijing Normal University, Beijing, China.

His research interests include the estimation of land surface net radiation from satellite data.